nature cancer

Article

https://doi.org/10.1038/s43018-025-00919-0

An antibody–toxin conjugate targeting CD47 linked to the bacterial toxin listeriolysin O for cancer immunotherapy

Received: 23 January 2024

Accepted: 22 January 2025

Benjamin R. Schrank[1,9], Yifan Wang[1,9], Annette Wu[1], Nhat Tran[2], DaeYong Lee[3,4], Jared Edwards[1], Kristin Huntoon[5], Shiyan Dong[1], JongHoon Ha[1], Yifan Ma[1], Adam J. Grippin[1], Seong Dong Jeong[6,7], Abin Antony[1], Mengyu Chang[1], Minjeong Kang[3], Thomas D. Gallup[6,7], Albert C. Koong[1], Jing Li[1], Kyuson Yun[2,8], Betty Y. S. Kim[6,7] ✉ & Wen Jiang[1] ✉

Antigen-presenting cells phagocytose tumor cells and subsequently cross-present tumor-derived antigens. However, these processes are impeded by phagocytosis checkpoints and inefficient cytosolic transport of antigenic peptides from phagolysosomes. Here, using a microbial-inspired strategy, we engineered an antibody–toxin conjugate (ATC) that targets the 'don't eat me' signal CD47 linked to the bacterial toxin listeriolysin O from the intracellular bacterium *Listeria monocytogenes* via a cleavable linker (CD47–LLO). CD47–LLO promotes cancer cell phagocytosis by macrophages followed by LLO release and activation to form pores on phagolysosomal membranes that enhance antigen cross-presentation of tumor-derived peptides and activate cytosolic immune sensors. CD47–LLO treatment in vivo significantly inhibited the growth of both localized and metastatic breast and melanoma tumors and improved animal survival as a monotherapy or in combination with checkpoint blockade. Together, these results demonstrate that designing ATCs to promote immune recognition of tumor cells represents a promising therapeutic strategy for treating multiple cancers.

Continual progress toward the development of more powerful antibody–drug conjugates (ADCs) has driven innovation in payload design ranging from cytotoxins to non-chemotherapeutics to immune-stimulating agents[1–4]. Targeting the cytosolic DNA sensor cGMP–AMP synthase (cGAS) and its downstream effector, the stimulator of interferon (IFN) genes (STING), within antigen-presenting cells (APCs) is one therapeutic strategy for generating tumor-specific T cell immunity[5–7]. Several STING agonists are currently in clinical development with varying degrees of success[8–11]. Nevertheless, at present, no ADCs in advanced development or approved for clinical use at this time specifically target cytosolic immune sensors or are designed to enhance APC functionalities.

Antibodies against the myeloid checkpoint CD47 may augment STING signaling in APCs via the escape of engulfed tumor double-stranded DNA from phagolysosomes[12]. Nevertheless, phagolysosomal escape is a highly inefficient, random process, and no specialized endogenous transporter has been identified that performs such a task[13]. Similarly, cross-presentation of neoantigens also requires

---

[1]Department of Radiation Oncology, The University of Texas MD Anderson Cancer Center, Houston, TX, USA. [2]Department of Neurology, Houston Methodist Research Institute, Houston, TX, USA. [3]Fralin Biomedical Research Institute at VTC, Virginia Tech, Roanoke, VA, USA. [4]Department of Biomedical Engineering and Mechanics, Virginia Tech, Blacksburg, VA, USA. [5]Department of Neurosurgery, the University of Arizona, Tucson, AZ, USA. [6]Department of Neurosurgery, The University of Texas MD Anderson Cancer Center, Houston, TX, USA. [7]Brain Tumor Center, The University of Texas MD Anderson Cancer Center, Houston, TX, USA. [8]Department of Neurology, Weill Cornell Medical College, New York, NY, USA. [9]These authors contributed equally: Benjamin R. Schrank, Yifan Wang. ✉e-mail: bykim@mdanderson.org; wjiang4@mdanderson.org

the release of cancer peptides from phagolysosomes into the cytosol, where they can be further processed by proteasomes and loaded onto major histocompatibility complex (MHC) molecules in the endoplasmic reticulum. Therefore, driving phagolysosomal escape of tumor cell components, whether they are nucleic acids or peptides, may stimulate a more robust and effective anti-tumor immune response.

L. monocytogenes survive phagolysosomal destruction to gain access to the cytosol by producing listeriolysin O (LLO), a non-enzymatic cytolysin activated by reducing agents and inhibited by oxidizing agents with maximum activity at pH 5.5 (refs. 14–16). In acidic phagosomes (pH ~5.9), LLO monomers oligomerize into arcs that fuse to form β-barrel channels in phagolysosome membranes[17]. Upon entry into the cytosol, LLO monomers are deprotonated and inactivated, thereby preserving cellular integrity. Liberated *L. monocytogenes* form a replicative niche in the host cell. Phagosomal release of bacterial nucleic acids and proteins drives Toll-like receptor (TLR) signaling, cGAS–STING activation and antigen presentation, which collectively facilitate T cell mobilization for pathogen clearance and long-term immunity to reinfection[18–20]. We hypothesized that LLO could similarly release engulfed cancer cell components into the cytosol and promote antigen presentation and cGAS–STING pathway activation for tumor immunity.

In this work, we engineered an ATC linking the anti-CD47 antibody to LLO, which we term CD47–LLO. We demonstrate that CD47–LLO increases tumor cell phagocytosis by macrophages and the cytosolic delivery of tumor peptides and DNA from phagolysosomes. Against multiple solid tumor models, CD47–LLO enhances therapeutic effectiveness compared with anti-CD47 antibody alone and shows synergistic effects when combined with anti-programmed cell death protein 1 (PD-1) therapy.

Results

Conjugation of LLO to anti-CD47 antibody

CD47–LLO is composed of the MIAP410 antibody modified with the click chemistry labeling reagent DBCO–PEG4–NHS ester, which we allowed to react with the LLO protein modified with the cross-linking reagent succinimidyl 3-(2-pyridyldithio)propionate (SPDP)–PEG11–azide (Fig. 1a and Extended Data Fig. 1a–d). Unconjugated antibody and LLO proteins were removed by affinity and size exclusion chromatographic methods, respectively (Fig. 1b,c). The coupling efficiency was determined by reducing 4–15% gradient sodium dodecyl sulfate polyacrylamide gel electrophoresis (SDS–PAGE) with 90% of the product showing a molar ratio of 1 LLO per anti-CD47 antibody (Fig. 1d).

In contrast to other pore-forming toxins, LLO is expressed by intracellular bacteria and preferentially accumulates within phagosomes by interacting with adaptor proteins involved in endocytosis[21]. However, extracellular LLO can induce pleiotropic effects on cholesterol-containing target membranes, including the formation of Ca^{2+} channels and large hemolytic pores[22,23]. We tested the β-hemolytic activity of CD47–LLO relative to unconjugated LLO and found that CD47–LLO triggered negligible levels of hemolysis (Fig. 1e). However, under reducing conditions, which allow disulfide bond reduction and LLO dissociation, the β-hemolytic activity of CD47–LLO approximated that of unconjugated LLO. Relative to unconjugated LLO, CD47–LLO did not induce cellular apoptosis or necrosis of bone marrow-derived macrophages (BMDMs) or various solid cancer cell lines (Fig. 1f and Extended Data Fig. 2a–h). These findings suggest that cross-linking anti-CD47 antibody with LLO via SPDP limits LLO activities to phagolysosomes, where the reducing and acidic environment allows disulfide bond cleavage and LLO activation (Fig. 1g).

CD47–LLO drives tumor phagocytosis and antigen presentation

To explore how CD47–LLO affects the effector functions of APCs, we co-cultured BMDMs and bone marrow-derived dendritic cells (BMDCs) with breast cancer cells. CD47–LLO, relative to corresponding controls including anti-CD47 antibody and isotype-matched immunoglobulin G (IgG)–LLO, consistently increased tumor cell phagocytosis by macrophages (Fig. 2a,b) and dendritic cells (DCs) (Extended Data Fig. 3a,b). The increase in CD47–LLO-driven phagocytosis was metabolically dependent (Fig. 2c,d). Because protumoral tumor-associated macrophages (TAMs) are typically alternatively activated[24], we asked whether BMDMs exposed to CD47–LLO could be reprogrammed to a pro-inflammatory state. We therefore compared CD86 and CD206 expression in BMDMs co-cultured with EO771 cells and treated with CD47–LLO. We also included another control: a noncleavable version of CD47–LLO (CD47–LLO-NC) that renders LLO unable to dissociate into a pore-forming monomer. Relative to anti-CD47 antibody and IgG–LLO, CD47–LLO increased the percentage of BMDMs with $CD86^+$ expression (Fig. 2e,f). By contrast, CD47–LLO-NC did not increase $CD86^+$ polarization. These results directly show that the release of LLO from CD47–LLO is critical to enhance macrophage activation to a pro-inflammatory phenotype.

Inside phagolysosomes, LLO oligomerizes into arcs that self-assemble into functional pores measuring 300–500 Å in diameter[25,26]. We next determined whether CD47–LLO disrupts phagolysosome membranes by visualizing BMDMs with transmission electron microscopy and quantifying intact vacuoles by using Icy bioimaging software and its HK-Means segmentation platform[27,28]. We also tracked the subcellular localization of internalized gold nanoparticles (Au-NPs) within BMDMs. Cross-sectional images of BMDMs revealed that, after anti-CD47 treatment, Au-NPs localized within double-membraned phagolysosomes (Fig. 2g). By contrast, after treatment with CD47–LLO, Au-NPs localized within the cytoplasm, BMDMs showed breaches in phagolysosome membranes and fewer intact vacuoles were quantified (Fig. 2h). To explore the effects of CD47–LLO on lysosomal pH, we stained BMDMs and BMDCs with LysoTracker Red and acridine orange (AO). Disruption of proton gradients decreases the efficiency of LysoTracker Red and AO lysosomal retention, which can be detected as a loss of LysoTracker Red staining and, in AO-stained cells, a metachromatic shift from red to green fluorescence. CD47–LLO decreased LysoTracker Red staining (Fig. 2i,j) and AO red staining (Fig. 2k–m and Extended Data Fig. 3c,d) in BMDMs and BMDCs. In sum, these results suggest that CD47–LLO disrupts APC lysosomes, providing a potential mechanism for the escape of endocytosed antigens.

To assess whether CD47–LLO can potentiate antigen presentation, we co-incubated BMDMs and BMDCs with EO771 cells that express the ovalbumin (OVA)-derived epitope SIINFEKL[29]. By using an antibody that recognizes SIINFEKL–H-2Kb complexes[30], we found low levels of OVA peptide presentation on MHC class I molecules after treatment with IgG, IgG–LLO or anti-CD47 antibody (Fig. 2n,o, Extended Data Fig. 3e,f and Supplementary Fig. 1). By contrast, SIINFEKL–H-2Kb complexes were significantly increased in BMDMs and BMDCs treated with CD47–LLO. To determine whether CD47–LLO can more efficiently prime antigen-specific T cells, we incubated BMDMs that had previously been co-cultured with OVA-expressing EO771 cells with $CD8^+$ T cells from OT-I transgenic mice. CD47–LLO treatment of BMDM–EO771 co-cultures increased the proliferation of OT-I T cells, whereas treatment of BMDMs co-cultured with T cells alone did not (Fig. 2p,q). These results suggest that CD47–LLO promotes tumor cell phagocytosis and lysosomal permeability, thereby enhancing tumor antigen cross-presentation and tumor-specific T cell priming.

CD47–LLO activates cGAS–STING and downstream effectors

Because release of phagolysosomal contents might also activate cytosolic DNA-sensing pathways, we explored cGAS–STING signaling in TAMs. We started with a 4T1Br4 triple-negative breast carcinoma model in which tumor cells were implanted subcutaneously within the mouse mammary fat pad and treated with intratumoral injection 6 d later (Extended Data Fig. 4a). Tumors treated with anti-CD47 antibody showed few TAMs and low levels of phosphorylated STING

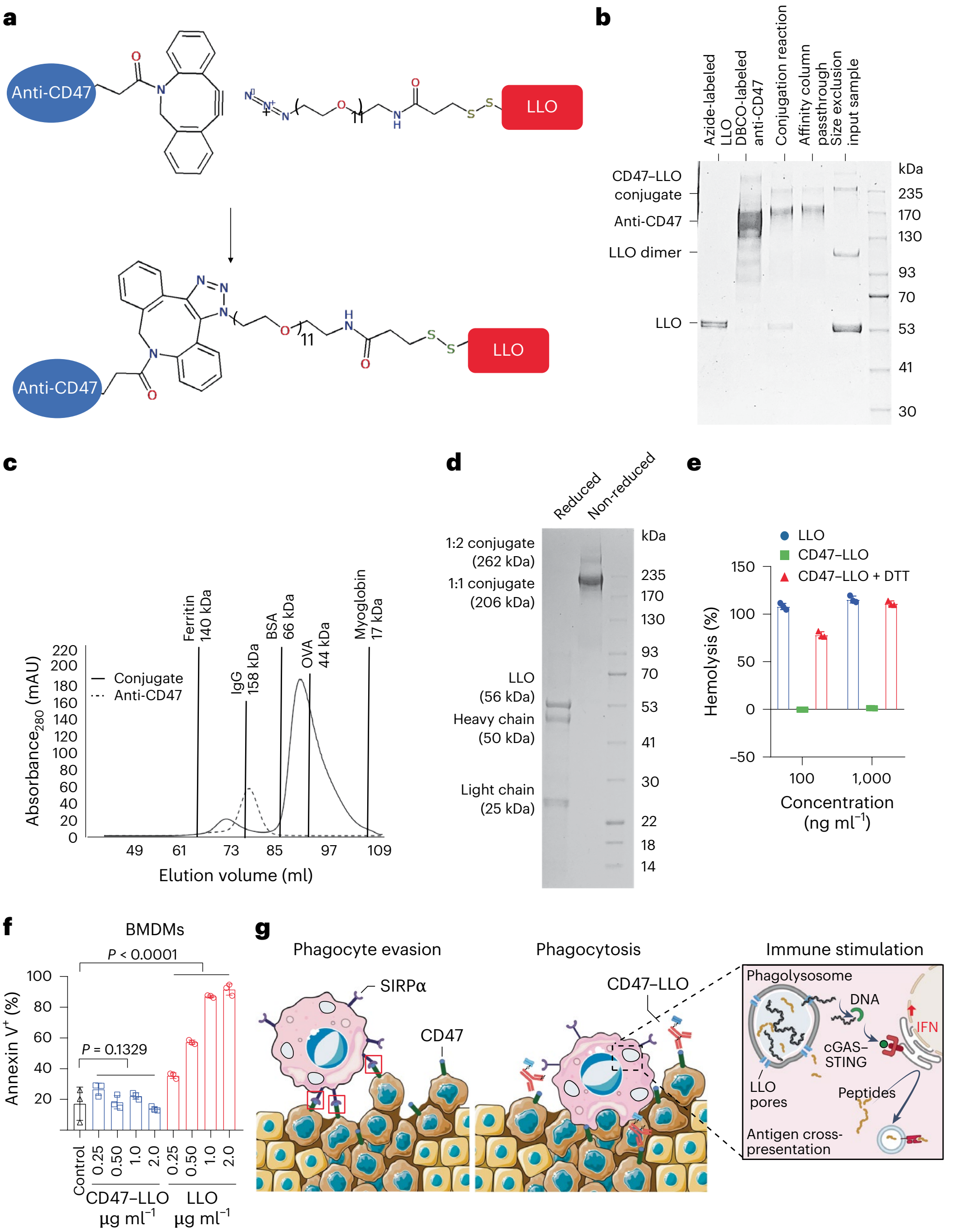

Fig. 1 | Conjugation and purification of anti-CD47 antibody with LLO. **a**, Schematic of antibody–toxin conjugation. The anti-CD47 antibody and LLO were modified by using the click chemistry labeling reagent DBCO–PEG4–NHS ester and the cross-linking reagent SPDP–PEG11–azide, respectively. The modified LLO protein was mixed with the antibody and allowed to react overnight at room temperature. Unconjugated antibody and LLO proteins were removed by affinity and size exclusion chromatographic methods, respectively. **b**, SDS–PAGE results of azide-labeled LLO, DBCO-labeled anti-CD47, the conjugation reaction, the affinity column passthrough and the size exclusion input sample. Experiment was repeated independently three times with similar results; a representative result is shown. **c**, Size exclusion chromatogram of conjugate (solid line) and anti-CD47 antibody alone (dashed line). Experiment was repeated independently three times with similar results; a representative result is shown. BSA, bovine serum albumin; mAU, milli-absorbance units. **d**, Representative SDS–PAGE results of conjugate in reductive and non-reductive loading buffers from $n = 3$ independent experiments. **e**, Hemolysis assay of LLO, CD47–LLO and CD47–LLO treated with reducing agent (5 mM dithiothreitol (DTT), 30 min) from $n = 3$ independent experiments. Hemolysis percentage was normalized to values from 0.1% Triton X-100. **f**, Apoptosis assay by flow cytometry of mouse BMDMs treated with CD47–LLO or LLO for 24 h from $n = 3$ independent experiments. **g**, Proposed mechanism of action of CD47–LLO. Tumor cells sidestep phagocytosis by amplifying expression of the 'don't eat me' signal, CD47 (red boxes, left). The anti-CD47 antibody promotes tumor cell phagocytosis by APCs (macrophages or DCs). Inside phagolysosomes, LLO monomers dissociate from anti-CD47 antibodies and form membrane permeations that allow tumor DNA and antigenic peptides to escape into the cytosol (inset, right). This in turn activates cGAS–STING to produce type I IFNs and enhance cross-presentation of neoantigens. SIRPα, signal regulatory protein α. Data shown represent mean ± s.d. (**e**,**f**) analyzed by one-way analysis of variance with Tukey's multiple-comparison test. $n = 3$ biologically independent experiments. Panel **g** created by modifying graphics from Servier Medical Art (https://smart.servier.com) licensed under CC BY 4.0 and BioRender.com.

(p-STING; Fig. 3a,b). By contrast, CD47–LLO increased infiltration of TAMs, which expressed p-STING at high levels (Fig. 3c). We verified that the expression of cGAS and p-STING was also upregulated in BMDMs and BMDCs co-cultured with EO771 breast carcinoma cells exposed to CD47–LLO (Fig. 3d–f, Extended Data Fig. 3g,h and Supplementary Fig. 2).

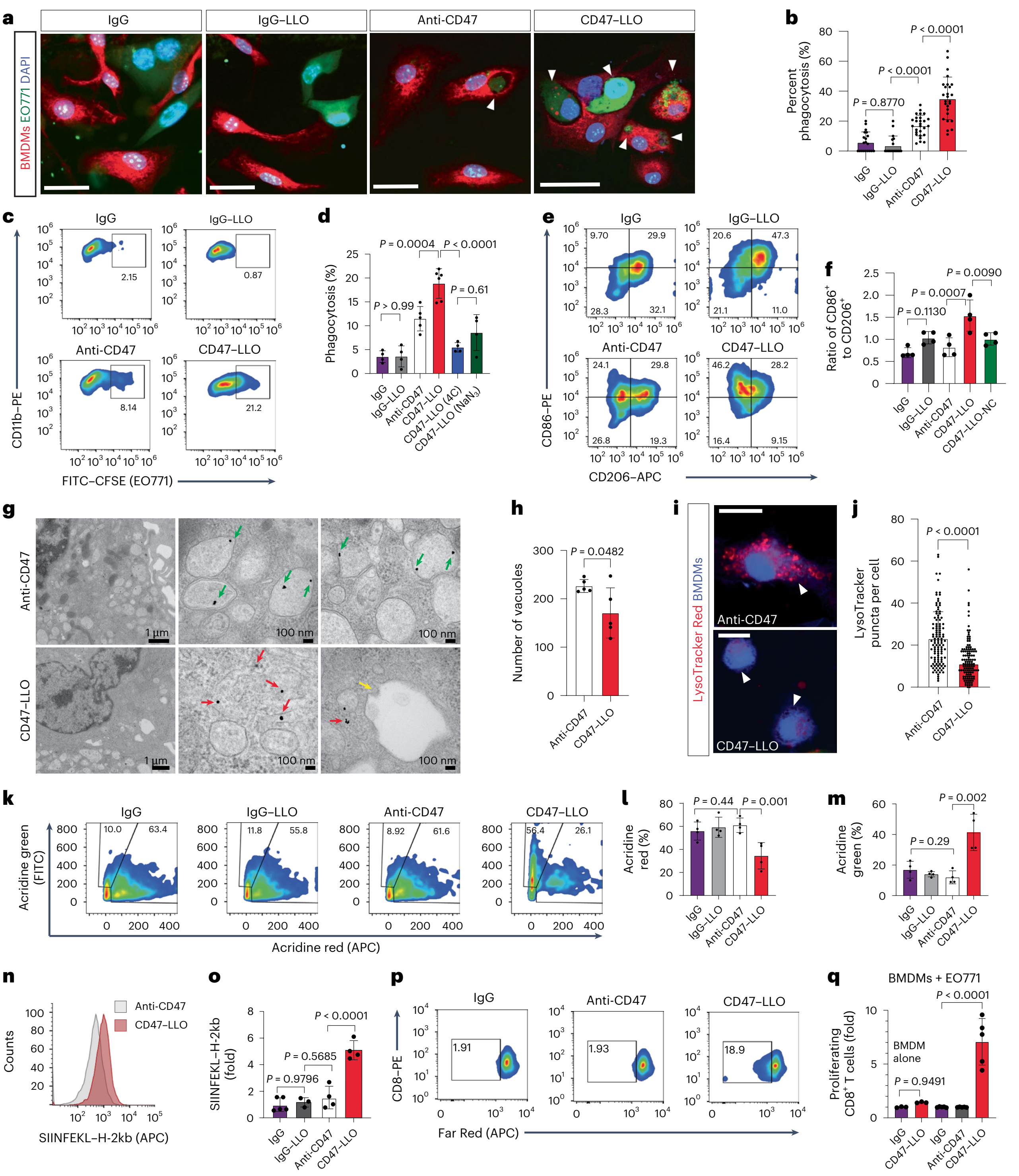

Fig. 2 | CD47–LLO promotes phagocytosis, lysosomal permeabilization and antigen presentation in vitro. a, Representative images of BMDM phagocytosis of EO771 cells (white arrowheads). Scale bars, 20 µm. DAPI, 4,6-diamidino-2-phenylindole. **b**, Quantification of BMDMs containing EO771 cells per field of view (*n* = 20 for IgG, *n* = 18 for IgG–LLO, *n* = 27 for anti-CD47 antibody, *n* = 26 for CD47–LLO from *n* = 3 independent experiments). **c**,**d**, Flow cytometry analysis (**c**) and quantification (**d**) of BMDM phagocytosis. *n* = 4 independent experiments for IgG, IgG–LLO, CD47–LLO (4 °C) and CD47–LLO (NaN$_3$). *n* = 5 for anti-CD47 antibody and *n* = 6 for CD47–LLO. CFSE, carboxyfluorescein succinimidyl ester. **e**,**f**, Flow cytometry analysis (**e**) and quantification (**f**) of CD86 and CD206 expression in BMDMs. *n* = 4 independent experiments. **g**, Transmission electron microscopy images of BMDMs with Au-NPs inside phagolysosomes (green arrows) or within the cytoplasm (red arrows). Yellow arrow shows wall perforation. **h**, Quantification of intact vacuoles; *n* = 5 independent experiments. **i**, Confocal images of BMDMs (white arrowheads) stained with LysoTracker Red. Scale bars, 20 µm. **j**, Quantification of LysoTracker Red puncta per BMDM (*n* = 114 for anti-CD47 antibody, *n* = 119 for CD47–LLO. *n* = 3 independent experiments). **k**, Flow cytometry analysis of BMDMs stained with AO. **l**,**m**, Quantification of acridine red (**l**) and acridine green (**m**) from *n* = 4 independent experiments. **n**,**o**, Flow cytometry analysis (**n**) and quantification (**o**) of SIINFEKL–H-2Kb peptide cross-presentation on BMDMs (*n* = 3 for IgG-LLO, *n* = 5 for IgG, *n* = 4 for other treatment groups). **p**,**q**, Flow cytometry analysis (**p**) and quantification (**q**) of OT-I CD8$^+$ T cell proliferation with (*n* = 5) or without (*n* = 3) EO771 cells. Data shown represent mean ± s.d. (**b**,**d**,**f**,**j**,**l**,**m**,**o**,**q**) or mean ± s.e.m. (**h**) analyzed by two-sided unpaired Student's *t*-tests (**h**,**j**) or one-way analysis of variance with Tukey's multiple-comparison test (**b**,**d**,**f**,**l**,**m**,**o**,**q**).

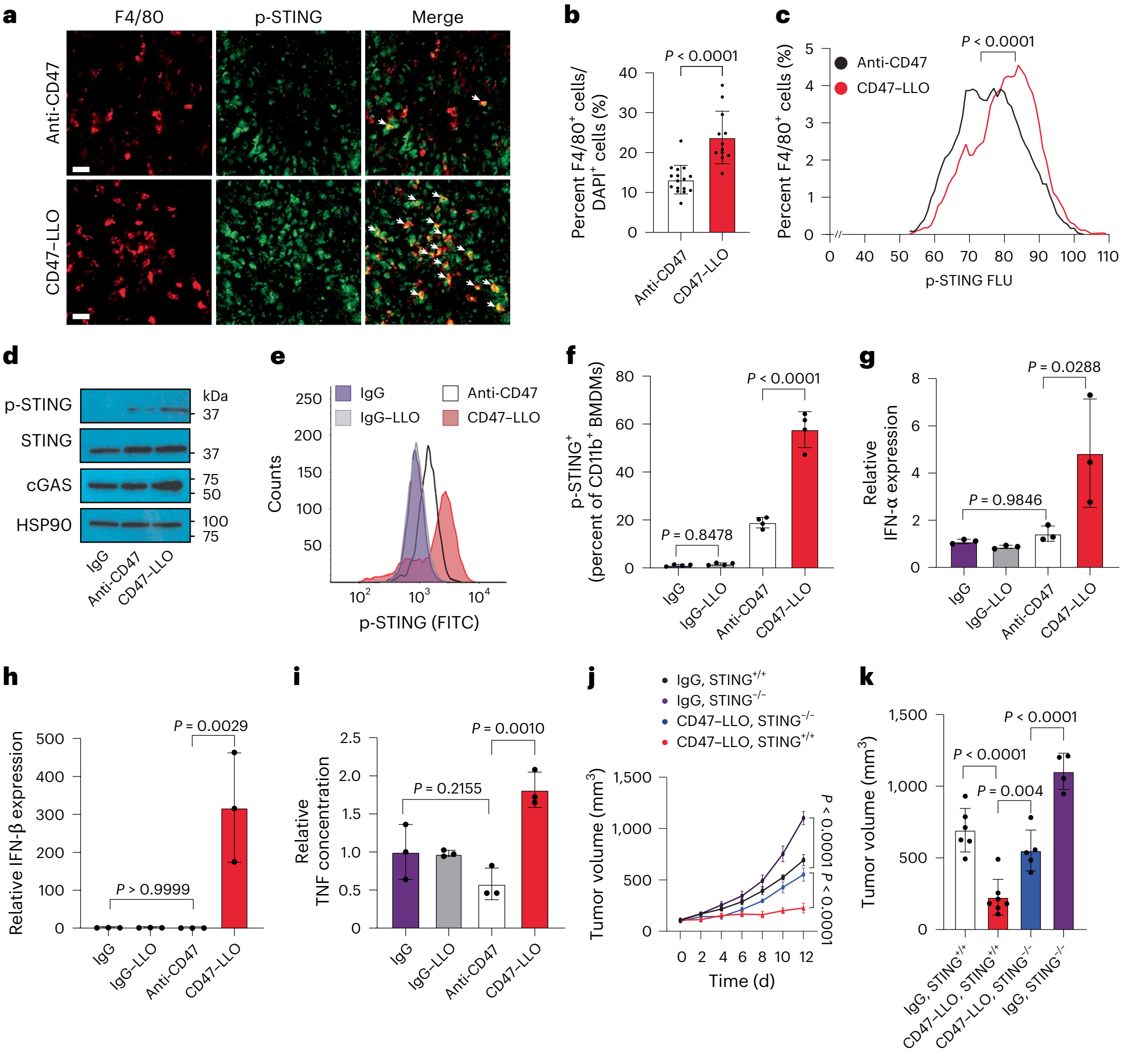

Fig. 3 | CD47–LLO activates STING signaling in vitro and in primary breast cancer in vivo. a, WT mice were inoculated with 4T1Br4 breast tumors and treated with intratumoral anti-CD47 antibody or CD47–LLO as described in Extended Data Fig. 4a. Representative images show levels of p-STING and macrophages (F4/80^{+}). Arrows show F4/80^{+} and p-STING^{+} co-labeled cells. Scale bar, 20 µm. **b**, Quantification of F4/80^{+} cells per DAPI^{+} cells per field of view ($n = 16$ for anti-CD47 antibody, $n = 12$ for CD47–LLO from $n = 3$ biologically independent tumors per condition). **c**, Distribution of p-STING fluorescence (FLU) intensity within F4/80^{+} cells. $n = 3$ biologically independent tumors per condition. **d**, Western blotting of proteins in the cGAS–STING pathway from BMDMs. A representative result is shown from $n = 3$ independent experiments. HSP90, heat shock protein 90. **e**,**f**, Flow cytometry analysis (**e**) and quantification (**f**) of p-STING levels in BMDMs isolated from EO771 co-cultures. $n = 4$ independent experiments. **g**, Real-time PCR results of *Ifna* expression levels in BMDMs. $n = 3$ independent experiments. **h**, Real-time PCR results of *Ifnb* expression levels in BMDMs. $n = 3$ independent experiments. **i**, TNF levels in cell culture supernatants ($n = 3$). **j**,**k**, WT or STING$^{-/-}$ mice were inoculated with EO771 breast tumor cells and treated with intratumoral IgG or CD47–LLO. Growth curves for EO771 breast tumors (**j**) and comparison of tumor volumes at day 12 (**k**) after intratumoral injection are shown (**j**). $n = 7$ for CD47–LLO-treated and $n = 6$ for IgG-treated WT mice; $n = 5$ for CD47–LLO-treated and $n = 4$ for IgG-treated STING$^{-/-}$ mice. Data shown represent mean ± s.e.m. (**b**,**j**) or mean ± s.d. (**f**–**i**,**k**) analyzed by two-sided unpaired Student's *t*-tests (**b**), one-way analysis of variance with Tukey's multiple-comparison test (**f**–**i**,**k**), two-way analysis of variance with Tukey's multiple-comparison test (**j**) or unpaired two-tailed Mann–Whitney *U*-test of the median value of p-STING intensity within F4/80^{+} cells (**c**).

We next sought to determine the functional consequences of cGAS–STING activation after CD47–LLO treatment. We explored the production of pro-inflammatory cytokines in BMDMs co-cultured with EO771 tumor cells and found that levels of IFN-α, IFN-β and tumor necrosis factor (TNF) were increased in BMDMs after CD47–LLO treatment (Fig. 3g–i). Next, we explored the extent to which the double-stranded DNA-sensing cGAS–STING pathway contributed to CD47–LLO's anti-tumor activity. We treated wild-type (WT) or STING$^{-/-}$ mice bearing orthotopically implanted EO771 tumors with CD47–LLO via intratumoral injection. STING depletion significantly reduced but did not completely abrogate the anti-tumor effect of CD47–LLO, emphasizing the contribution of complementary pathways including tumor cell phagocytosis and antigen presentation in driving CD47–LLO anti-tumor activity (Fig. 3j,k).

CD47–LLO drives antigen-specific anti-tumor immunity in vivo

To decouple the anti-tumor effect of the myeloid checkpoint inhibitor anti-CD47 antibody from CD47–LLO, we elected to focus on syngeneic orthotopic breast cancer models and the D4M.3A syngeneic orthotopic melanoma model, which harbors a *Braf* mutation[31]. In both the 4T1Br4 and EO771 breast cancer models, intratumoral delivery of CD47–LLO significantly enhanced primary tumor control relative to anti-CD47 antibody (Fig. 4a,b, Extended Data Fig. 4b and Supplementary Fig. 3). Notably, EO771 breast tumors were resistant to treatment with IgG–LLO and the noncleavable version of CD47–LLO, again demonstrating the distinct requirement for phagocytosis and LLO release in our model system. In the D4M.3A model, treatment with CD47–LLO also led to greater local tumor control (Fig. 3c) and improved survival in comparison with mice treated with anti-CD47 antibody (Fig. 3d).

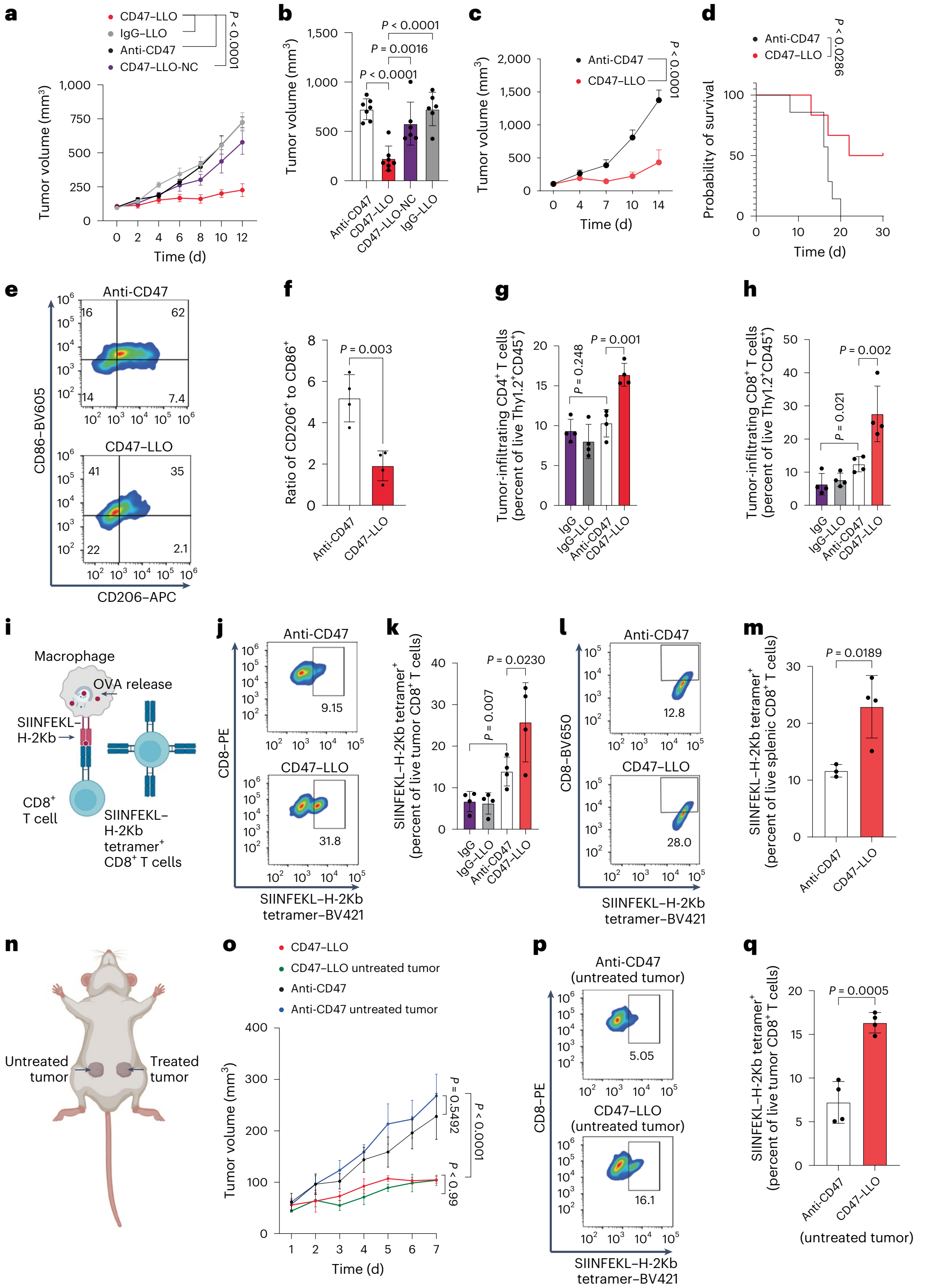

Fig. 4 | CD47–LLO drives tumor antigen-driven T cell responses in vivo. **a**,**b**, WT female mice were inoculated with EO771 breast tumors and treated with intratumoral anti-CD47 antibody, CD47–LLO, IgG–LLO or a noncleavable CD47–LLO-NC conjugate (Supplementary Fig. 3a). Tumor volumes were monitored and analyzed for the indicated periods (**a**) and quantified at day 12 after tumor inoculation (**b**). $n = 6$ for IgG–LLO, $n = 6$ CD47–LLO-NC and $n = 7$ for all remaining groups. **c**, D4M.3A tumor volumes (Supplementary Fig. 3b). $n = 6$ for all groups. **d**, Survival curves for each treatment group. $n = 6$ for CD47–LLO and $n = 7$ for anti-CD47 antibody. **e**,**f**, Flow cytometry analysis (**e**) and quantification (**f**) of CD86$^+$ and CD206$^+$ TAMs in 4T1Br4 tumors. $n = 4$ biologically independent experiments. **g**,**h**, Quantification of CD4$^+$ (**g**) and CD8$^+$ (**h**) cells in EO771 tumors. $n = 4$ biologically independent tumors per condition. **i**, Schematic illustrating the mechanism of SIINFEKL–H-2Kb tetramer$^+$CD8$^+$ T cell expansion. **j**,**k**, Flow cytometry analysis (**j**) and quantification (**k**) of SIINFEKL–H-2Kb tetramer$^+$CD8$^+$ T cells ($n = 4$ biologically independent tumors per condition). **l**,**m**, Flow cytometry analysis (**l**) and quantification (**m**) of SIINFEKL–H-2Kb tetramer$^+$CD8$^+$ T cells within the spleen ($n = 3$ for anti-CD47 and $n = 4$ for CD47-LLO). **n**, Schematic illustrating the bilateral breast tumor model. **o**, Treated and untreated tumor growth curves. $n = 7$ for anti-CD47; $n = 8$ for CD47-LLO treated tumors; $n = 6$ for all remaining groups. **p**,**q**, Flow cytometry analysis (**p**) and quantification (**q**) of SIINFEKL–H-2Kb tetramer$^+$CD8$^+$ T cells within the untreated tumor ($n = 4$ biological replicates). Data shown represent mean ± s.e.m. (**a**,**c**,**o**) or mean ± s.d. (**b**,**f**–**h**,**k**,**m**,**q**) analyzed by two-sided unpaired Student's *t*-test (**d**,**f**,**m**,**q**), one-way analysis of variance with Tukey's multiple-comparison test (**b**,**g**,**h**,**k**), two-way analysis of variance with Tukey's multiple-comparison test (**a**,**c**,**o**) or two-sided log-rank (Mantel–Cox) test (**d**). Figure 3j is reproduced in **a** to enable direct comparison of the data. Panels **i**,**n** created by modifying graphics from BioRender.com.

We next explored the innate and adaptive immune cells mobilized by CD47–LLO treatment. Noting our observed increases in CD86$^+$ polarized macrophages after CD47–LLO treatment in vitro (Fig. 2e,f), we found significant enrichment in CD86$^+$ tumor-infiltrating macrophages in vivo (Fig. 4e,f). Further analyses of T cell subsets revealed that numbers of tumor-infiltrating CD4$^+$ (Fig. 4g and Extended Data Fig. 4c) and CD8$^+$ (Fig. 4h and Extended Data Fig. 4d) T cells were elevated after CD47–LLO therapy compared with IgG, IgG–LLO or anti-CD47 treatment. Analysis of the OVA tetramer in CD8$^+$ T cells showed that CD47–LLO treatment promoted the generation of antigen-specific CD8$^+$ T cells within the tumor and spleen (Fig. 4i–m and Extended Data Fig. 4e). To assess whether CD47–LLO treatment could evoke systemic anti-tumor immunity, we established bilateral breast tumors in C57BL/6 mice and compared untreated tumors with tumors treated directly with anti-CD47 antibody or CD47–LLO (Fig. 4n). Bilateral tumors grew rapidly despite anti-CD47 treatment (Fig. 4o). By contrast, CD47–LLO suppressed the growth of both treated and untreated tumors, which were enriched in OVA-specific CD8$^+$ T cells (Fig. 4p,q). The biodistribution of fluorophore-tagged CD47–LLO confirmed that the near-infrared fluorescence signal of CD47–LLO was retained within the treated tumor for long periods without passively accumulating in the untreated tumor (Extended Data Fig. 5a–d). Collectively, these findings demonstrate that CD47–LLO promotes pro-inflammatory macrophage polarization and the robust intratumoral accumulation of tumor-specific T cells.

Transcriptomics reveals anti-tumor macrophage signatures

To define the identities of innate and adaptive immune cells that accumulate in tumors upon CD47–LLO treatment, we performed single-cell RNA sequencing (scRNA-seq) on CD45$^+$ cells isolated from EO771 tumors. CD45$^+$ cells were rare in IgG- or anti-CD47-treated animals (Fig. 5a,b). By contrast, we observed a 30-fold increase in CD45$^+$ cells upon CD47–LLO treatment. After rigorous quality control (Supplementary Fig. 4 and the Methods), we used our previously published methods[32] to annotate cells and interpret changes in their abundance and gene expression ($n = 13{,}891$ cells in total). We projected the data into two dimensions using uniform manifold approximation and projection (UMAP) mapping. Unsupervised clustering revealed 18 clusters of cells (Extended Data Fig. 6). We found that the CD45$^+$ population in IgG- and anti-CD47-treated tumors contained mostly macrophages, whereas CD47–LLO-treated tumors showed an increase in granulocytes (Fig. 5c,d). Tumor-associated neutrophil enrichment was validated by positive Ly6G and CD11b staining (Extended Data Fig. 7a,b). To characterize granulocyte expression signatures and population heterogeneity with higher resolution, we reanalyzed the data, performed unsupervised reclustering and obtained six populations (Extended Data Fig. 7c–g). In clusters 1–3, we observed distinct transcriptional signatures with genes supporting increased tumor-associated neutrophil functions including granule production (*Lcn2*), NO synthesis (*Nos2*) and IFN signaling (*Irf1*, *Sell*). In cluster 6, we further noted an increased MHC-II signature including *Cd74*, *H2-Ab1* and *H2-Eb1*. These results are in line with recent observations that immunotherapies that specifically target adaptive immune checkpoints can also recruit and activate neutrophils[33–35].

Given that proportionally low numbers of macrophages were represented in the CD45$^+$ population in the CD47–LLO treatment groups and to further define differences in macrophage populations important for EO771 tumor elimination, we reanalyzed the data, performed unsupervised reclustering and obtained ten TAM populations (Fig. 5e). We used prior published references[36,37] to identify clusters closely aligned with classical tumor-infiltrating macrophages (*Ccr2*$^{\mathrm{hi}}$, *Fn1*$^{\mathrm{hi}}$, *Cxcl10*$^{\mathrm{hi}}$), regulatory macrophages (*Arg1*$^{\mathrm{hi}}$, *Apoe*$^{\mathrm{hi}}$, *C1qa*$^{\mathrm{hi}}$), nonclassical monocytes (*Ace*$^{\mathrm{hi}}$, *Adgre4*$^{\mathrm{hi}}$, *Cd300a*$^{\mathrm{hi}}$) and resolution-phase macrophages (*H2-Aa*$^{\mathrm{hi}}$, *H2-Ab1*$^{\mathrm{hi}}$, *H2-Eb1*$^{\mathrm{hi}}$, *Cd74*$^{\mathrm{hi}}$) within IgG-, anti-CD47- and CD47–LLO-treated tumors (Fig. 5f,g and Extended Data Fig. 8a). Consistent with the dual functionality of CD47–LLO as a myeloid checkpoint inhibitor and activator of cytosolic nucleic acid sensors, CD47–LLO TAMs in clusters 1–3, and 5–10 were highly enriched in phagocytosis and type I IFN-related genes (Fig. 5h,i). We further observed that most of the macrophages in the CD47–LLO group were grouped in a distinct cluster, 'cluster 9', which represented fewer than 5% of cells in the anti-CD47 and IgG groups (Fig. 6a,b). Cluster 9 showed preferential expression of genes involved with neutrophil chemotaxis as well as lymphocyte recruitment, activation and antigen presentation including *Cxcl2*, *Ccl3*, *S100a8*, *S100a9*, *H2-Ab1*, *H2-Aa*, *Cd86* and *Cd80* (Extended Data Fig. 8b). Cluster 9 also showed an enrichment in gene ontology pathways including TLR signaling, NOD-like receptor signaling and lymphocyte activation (Fig. 6c and Extended Data Fig. 8c). These results suggest that, in addition to activating the cGAS–STING pathway and phagocytosis, CD47–LLO promotes a distinct TAM population most closely resembling inflammatory macrophages that bridge innate and adaptive immune responses.

CD47–LLO drives APC–T cell clustering and cross-talk

Professional APCs generate tumor-specific adaptive immune responses by directly engaging CD4$^+$ and CD8$^+$ T cells[38,39]. Because CD47–LLO enhanced tumor antigen presentation by BMDMs and BMDCs, we monitored APC recruitment and intratumoral localization with lymphocytes. In situ confocal microscopy revealed that F4/80$^+$, CD11c$^+$, CD4$^+$ and CD8$^+$ cells were diffusely scattered in the breast tumor parenchyma after anti-CD47 treatment (Figs. 3a,b and 6d–g). By contrast, CD47–LLO induced the influx of these cells, with CD11c$^+$, CD4$^+$ and CD8$^+$ cells forming spatially positioned triad clusters. CD8$^+$ and CD4$^+$ T cell localization within CD11c$^+$ triads was significantly increased with CD47–LLO treatment relative to anti-CD47 treatment, suggesting more efficient lymphocyte cooperation (Fig. 6h).

To explore cell type-specific immunomodulatory interactions between APCs and adaptive immune cells, we followed prior published references[40] to annotate functional subtypes of tumor-associated lymphocytes in terms of their gene expression signatures (Fig. 6i). By using CellChat, we analyzed our scRNA-seq data to identify ligand–receptor pairs, allowing us to infer putative cell-to-cell cross-talk[41,42]. Analysis of the immune populations involved in this study revealed both incoming and outgoing interactions between lymphocytes, macrophages

Fig. 5 | Transcriptome analysis reveals CD47–LLO TAM pro-inflammatory signatures. **a**–**i**, EO771 tumors were collected on day 3 after intratumoral treatment with IgG ($n = 3$), anti-CD47 antibody ($n = 4$) or CD47–LLO ($n = 4$) and subjected to fluorescence-activated cell sorting of CD45$^+$ cells. Cells were fixed, and 100,000 CD45$^+$ cells per tumor were pooled into the respective treatment groups and subjected to scRNA-seq. **a**,**b**, Flow cytometry analysis (**a**) and quantification (**b**) of CD45$^+$ cells isolated from EO771 tumors treated with intratumoral IgG, anti-CD47 antibody or CD47–LLO. $n = 3$ biological replicates. FITC, fluorescein isothiocyanate. **c**, UMAP mapping of 13,891 single cells from three treatment groups shows the composition of different cell types. UMAP projections are shown by assignment (**c**) and by sample (**d**). NK, natural killer. **e**, UMAPs of only macrophages color coded by cluster. **f**, Top 20 differentially expressed genes in ten macrophage clusters ranked by false discovery rate. Gene expression values were centered, scaled and transformed to a scale of −2 to 2. **g**, UMAP projection of macrophage populations showing the distribution of transcriptional signatures of predefined macrophage and monocyte subsets. Inset shows a dot plot depicting the average expression and percent expression of signature genes per macrophage cluster. **h**, Heatmap depicting expression of cGAS–STING pathway-related genes in macrophage clusters by treatment group and cluster. **i**, Heatmap depicting expression of phagocytosis-related genes in macrophage clusters by treatment group and cluster. Data shown represent mean ± s.d. (**b**) analyzed by one-way analysis of variance with Tukey's multiple-comparison test.

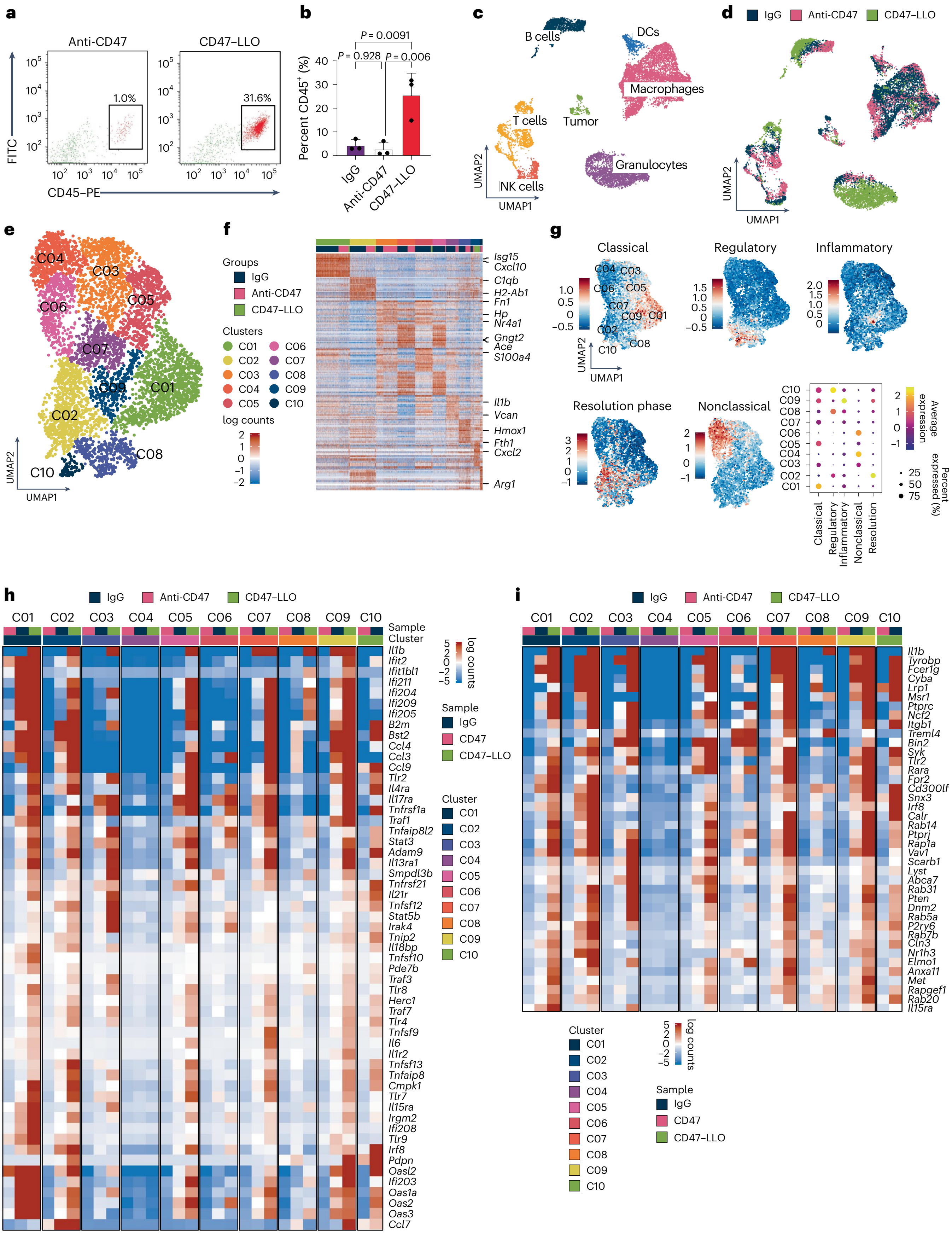
a
Anti-CD47
CD47–LLO
1.0%
31.6%
FITC
CD45–PE
10^2 10^3 10^4 10^5
b
P = 0.0091
P = 0.928
P = 0.006
Percent CD45$^+$ (%)
IgG
Anti-CD47
CD47–LLO
c
B cells
DCs
Macrophages
T cells
Tumor
Granulocytes
NK cells
UMAP1
UMAP2
d
IgG
Anti-CD47
CD47–LLO
e
C01 C02 C03 C04 C05 C06 C07 C08 C09 C10
f
Groups
IgG
Anti-CD47
CD47–LLO
Clusters
log counts
Isg15
Cxcl10
C1qb
H2-Ab1
Fn1
Hp
Nr4a1
Gngt2
Ace
S100a4
Il1b
Vcan
Hmox1
Fth1
Cxcl2
Arg1
g
Classical
Regulatory
Inflammatory
Resolution phase
Nonclassical
Average expression
Percent expressed (%)
25
50
75
Classical
Regulatory
Inflammatory
Nonclassical
Resolution
h
IgG
Anti-CD47
CD47–LLO
Sample
Cluster
log counts
Sample
IgG
CD47
CD47–LLO
Il1b
Ifit2
Ifit1bl1
Ifi211
Ifi204
Ifi209
Ifi205
B2m
Bst2
Ccl4
Ccl3
Ccl9
Tlr2
Il4ra
Il17ra
Tnfrsf1a
Traf1
Tnfaip8l2
Stat3
Adam9
Il13ra1
Smpdl3b
Tnfrsf21
Il21r
Tnfsf12
Stat5b
Irak4
Tnip2
Il18bp
Tnfsf10
Pde7b
Traf3
Tlr8
Herc1
Traf7
Tlr4
Tnfsf9
Il6
Il1r2
Tnfsf13
Tnfaip8
Cmpk1
Tlr7
Il15ra
Irgm2
Ifi208
Tlr9
Irf8
Pdpn
Oasl2
Ifi203
Oas1a
Oas2
Oas3
Ccl7
i
IgG
Anti-CD47
CD47–LLO
Il1b
Tyrobp
Fcer1g
Cyba
Lrp1
Msr1
Ptprc
Ncf2
Itgb1
Treml4
Bin2
Syk
Tlr2
Rara
Fpr2
Cd300lf
Snx3
Irf8
Calr
Rab14
Ptprj
Rap1a
Vav1
Scarb1
Lyst
Abca7
Rab31
Pten
Dnm2
Rab5a
P2ry6
Rab7b
Cln3
Nr1h3
Elmo1
Anxa11
Met
Rapgef1
Rab20
Il15ra
Cluster
log counts
Sample
IgG
CD47
CD47–LLO

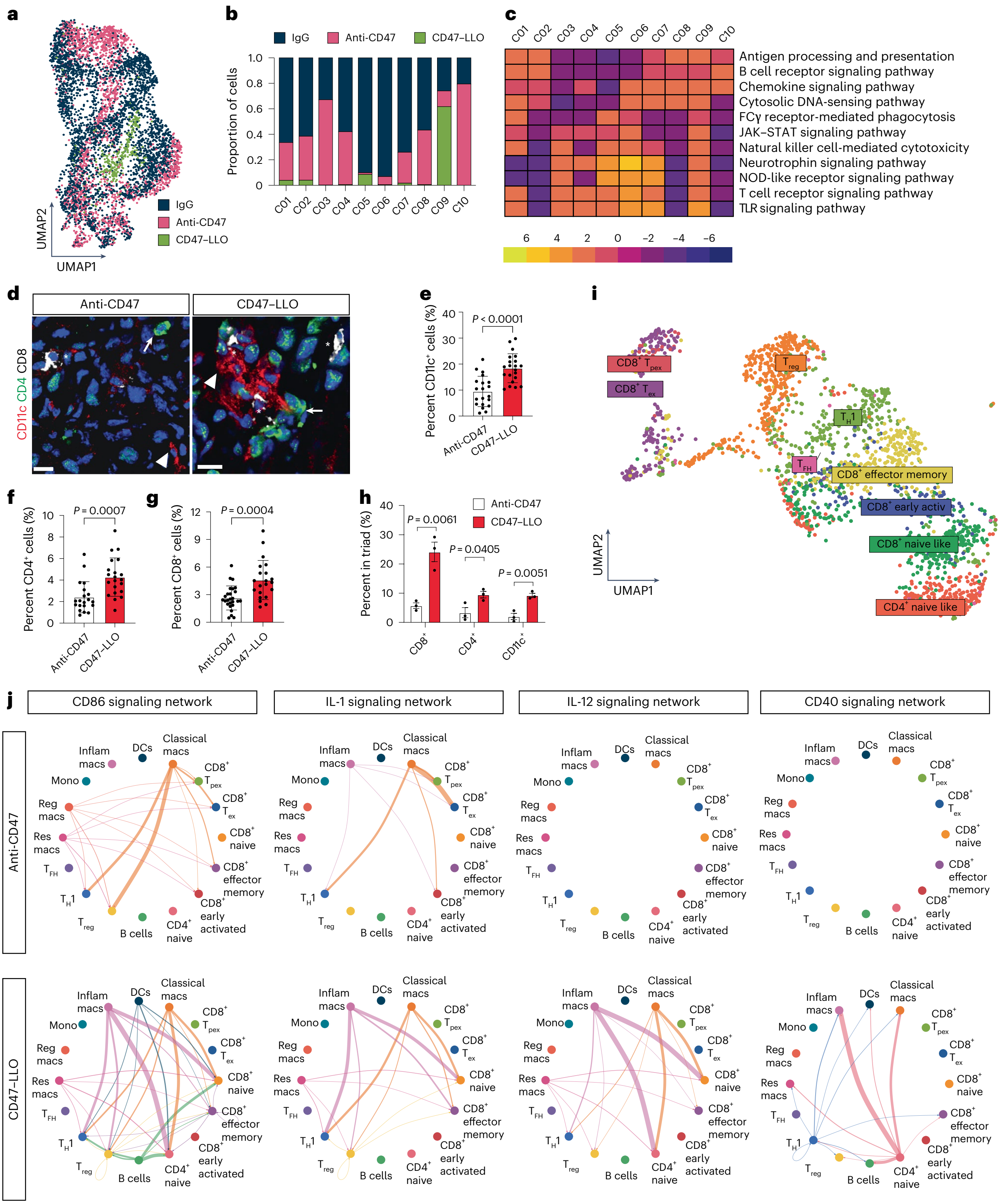

Fig. 6 | CD47–LLO facilitates innate and adaptive cell clustering and signaling in vivo. a, UMAP of macrophage populations isolated from EO771 tumors after intratumoral treatment with IgG ($n = 3$), anti-CD47 antibody ($n = 4$) or CD47–LLO ($n = 4$). **b**, Fraction of cells (y axis) from each cluster (x axis) color coded by sample. **c**, Heatmap displaying select upregulated and downregulated pathways from Kyoto Encyclopedia of Genes and Genomes gene set enrichment analysis. JAK, Janus kinase; STAT, signal transducer and activator of transcription. **d**, CD11c$^+$ cells (arrowheads), CD4$^+$ cells (arrows) and CD8$^+$ cells (asterisks) in 4T1Br4 tumors. Scale bar, 10 µm. **e**–**g**, Percentage of CD11c$^+$ cells (**e**), CD4$^+$ cells (**f**) and CD8$^+$ cells (**g**) per field of view from $n = 3$ biologically independent tumors per condition. **h**, Quantification of percentages of cells that colocalized in triad clusters from $n = 3$ independent experiments. **i**, UMAP projection of lymphocyte populations showing the distribution of predefined T cell subsets from the three treatment groups. Activ, activated; T$_{FH}$, follicular helper T cell; T$_H$1, type 1 helper T cell; T$_{reg}$, regulatory T cell; T$_{pex}$, progenitor exhausted T cell; T$_{ex}$, exhausted T cell. **j**, Cell-to-cell communication networks inferred with CellChat software. The strength of cell-to-cell interactions is represented in the edge width. Inflam, inflammatory; macs, macrophages; mono, monocytes; reg, regulatory. Data shown represent mean ± s.d. (**e**–**h**) analyzed by two-sided unpaired Student's t-test (**e**–**h**).

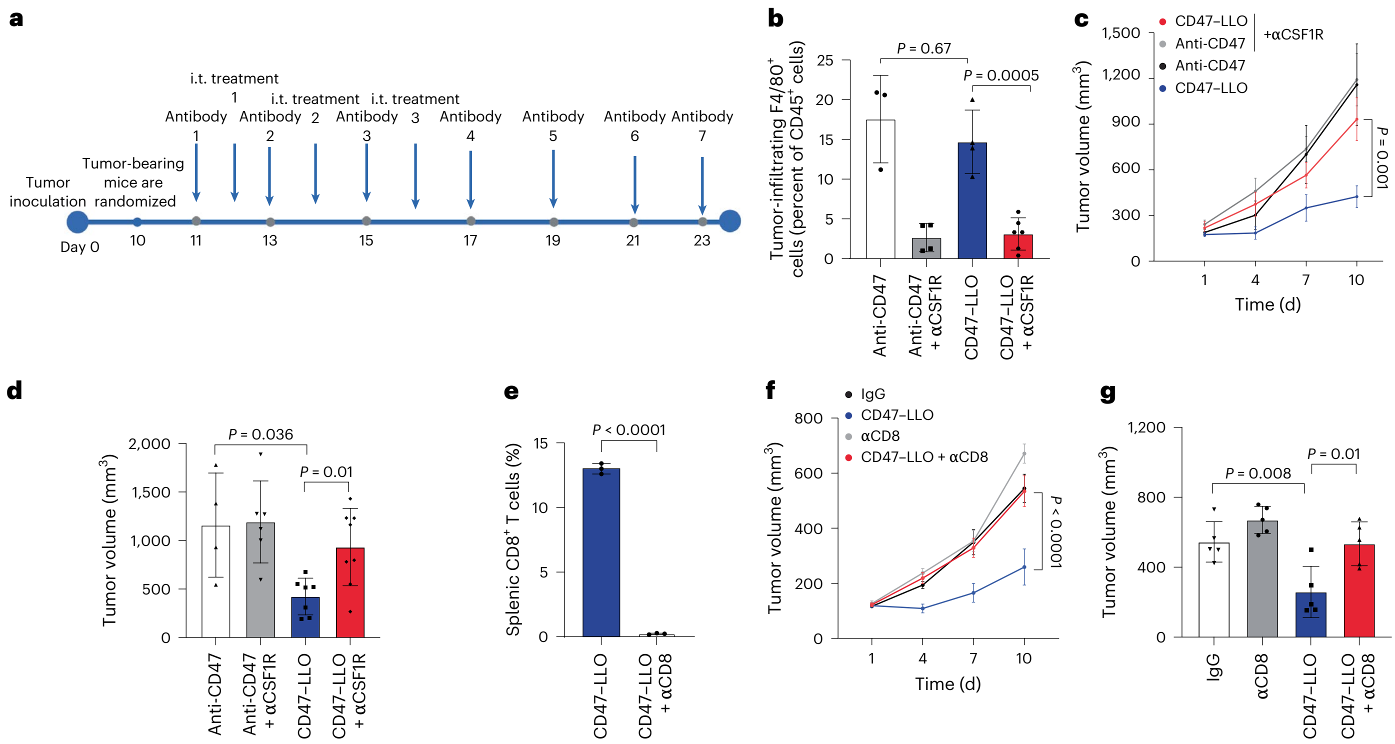

Fig. 7 | CD47–LLO requires macrophages and CD8$^+$ T cells for tumor cell elimination. a, Schematic for generating F4/80- or CD8-depleted mice and subsequent treatment with intratumoral (i.t.) CD47–LLO or anti-CD47 antibody. **b**, Efficiency of F4/80$^+$ cell depletion was evaluated ex vivo in mouse tumors after treatment with anti-CD47 antibody ($n = 3$), CD47–LLO ($n = 4$), anti-CD47 antibody and anti-CSF1R antibody ($n = 4$) or CD47–LLO and anti-CSF1R antibody ($n = 6$). **c**,**d**, Tumor volumes were monitored and analyzed for the indicated periods (**c**) and quantified at 10 d after treatment initiation (**d**). For anti-CSF1R (αCSF1R)-treated animals, $n = 6$ for anti-CD47 antibody and $n = 8$ for CD47–LLO. For IgG-treated animals, $n = 4$ for anti-CD47 antibody and $n = 7$ for CD47–LLO. **e**, Efficiency of CD8$^+$ T cell depletion was evaluated ex vivo in mouse spleens after treatment with CD47–LLO with and without anti-CD8 antibody. Data show $n = 3$ C57BL/6 mice per treatment group. **f**,**g**, Tumor volumes were monitored and analyzed for the indicated periods (**f**) and quantified at 10 d after treatment initiation (**g**). $n = 5$ for all treatment groups. Data shown represent mean ± s.e.m. (**c**,**f**) or mean ± s.d. (**b**,**d**,**e**,**g**) analyzed by one-way analysis of variance with Tukey's multiple-comparison test (**b**,**d**,**e**,**g**) or two-way analysis of variance with Tukey's multiple-comparison test (**c**,**f**).

and DCs within EO771 tumors (Fig. 6j). This included strong outgoing CD86 signaling from inflammatory macrophages and DCs to CD8$^+$ and CD4$^+$ T cells in CD47–LLO-treated tumors, corroborating our prior observations (Fig. 4e,f). Inflammatory macrophages further showed increased interleukin (IL)-1 and IL-12 signaling in CD47–LLO-treated tumors relative to ones treated with anti-CD47 antibody, highlighting potential axes contributing to CD4$^+$ and CD8$^+$ T cell accumulation and activation. We also observed increased CD40 outgoing signals from T cells to APCs, suggesting reciprocal feedback that enhances APC functionalities such as cytokine production and antigen presentation.

To investigate whether the anti-tumor effect of CD47–LLO was a consequence of bridging between innate and adaptive immune responses, we depleted intratumoral macrophages in vivo using an anti-CSF1R antibody (Fig. 7a,b). Relative to WT animals, tumors in macrophage-depleted mice grew rapidly despite CD47–LLO treatment (Fig. 7c,d). Similarly, depletion of intratumoral CD8$^+$ T cells with an anti-CD8 antibody also significantly diminished the anti-tumor effect of CD47–LLO (Fig. 7e–g). These observations collectively demonstrate the requirement for TAMs and CD8$^+$ T cells for effective tumor cell elimination by CD47–LLO.

CD47–LLO curbs the metastasis of aggressive breast tumors

We next elected to focus on the development of metastases in a highly aggressive model of triple-negative breast cancer. We treated mice bearing orthotopically implanted, spontaneously metastatic 4T1Br4 tumors with anti-CD47 antibody or CD47–LLO via intratumoral injection. Mice treated with anti-CD47 antibody rapidly grew distant metastases despite primary tumor resection, as evidenced by bioluminescence imaging (Fig. 8a,b). By contrast, we found that CD47–LLO decreased systemic disease progression. Only mice that received intratumoral CD47–LLO had extended survival (Fig. 8c), with complete tumor eradication observed in four of the seven mice.

Given that IFN production is known to induce the expression of immune checkpoints, we measured the expression of PD-1 in T cells and programmed cell death ligand 1 (PD-L1) in tumor cells. We found that, in CD47–LLO-treated mice, intratumoral CD8$^+$ T cells showed elevated expression of PD-1 (Fig. 8d,e) and increased expression of PD-L1 in tumors (Fig. 8f,g). We therefore asked whether the use of CD47–LLO in combination with immune checkpoint blockade would improve systemic disease progression. When delivered by intraperitoneal injection, combined CD47–LLO and anti-PD-1 antibody drove significant enrichment of CD8$^+$ T cells in 4T1Br4 tumors with decreased PD-1 expression (Fig. 8h,l and Extended Data Fig. 9a–c). All groups of mice except those treated with CD47–LLO and anti-PD-1 antibody rapidly grew distant metastases (Fig. 8j,k). In contrast to intratumoral injection, our assessment of CD47–LLO biodistribution showed that most of the CD47–LLO conjugate delivered by intraperitoneal injection accumulated in the liver, which probably contributed to a more modest therapeutic response (Extended Data Fig. 5e–g). Only mice that received combined CD47–LLO and anti-PD-1 antibody had an increase in survival (Fig. 8l), with complete tumor eradication observed in four of the six mice.

Administration of CD47–LLO by intraperitoneal injection was found to have mild toxicity, with stable body weight gain and no long-term hematologic, renal or hepatic toxicities (Extended Data Fig. 10a–e). Hematoxylin- and eosin-stained paraffin sections of major

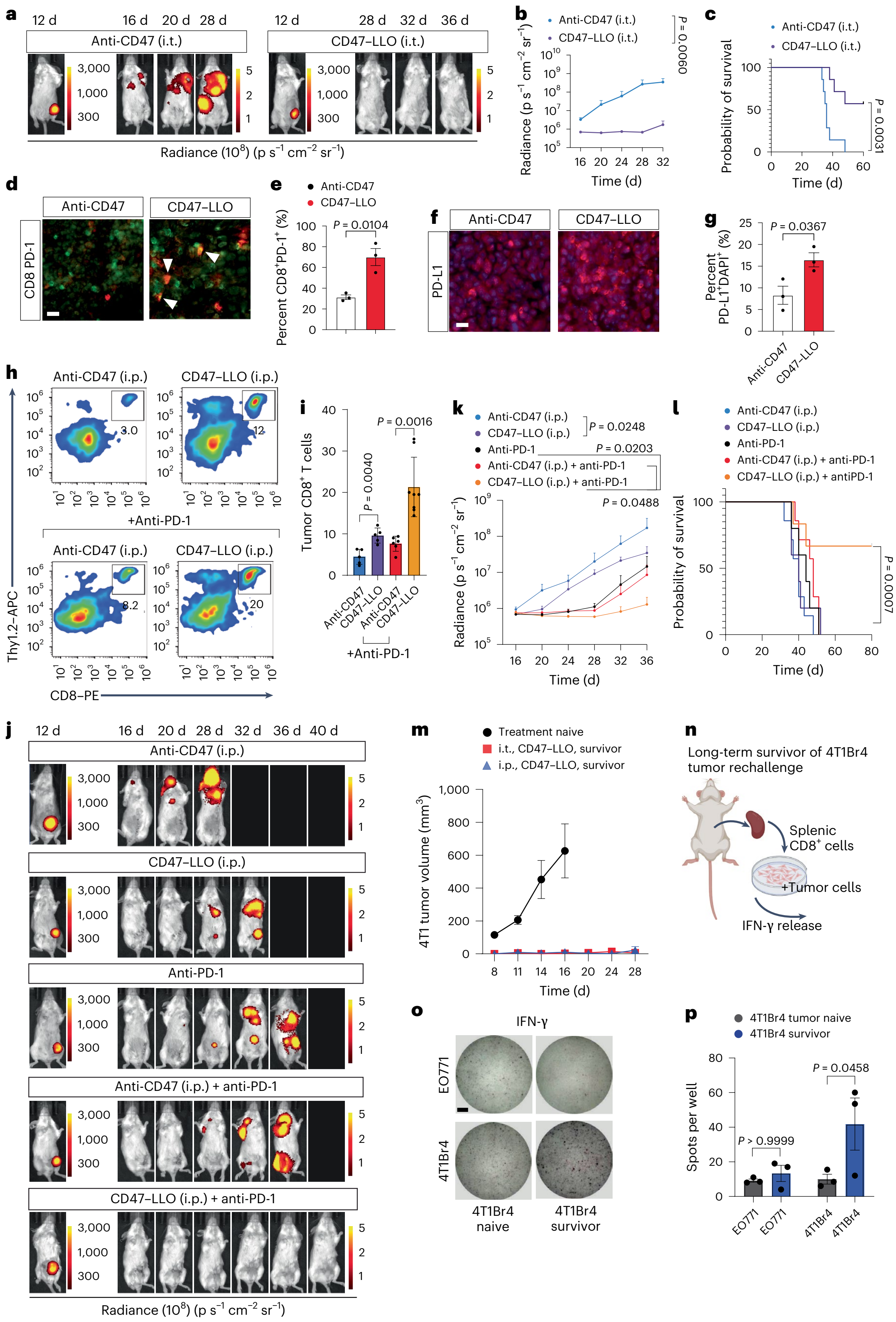
a
12 d
16 d
20 d
28 d
Anti-CD47 (i.t.)
12 d
28 d
32 d
36 d
CD47–LLO (i.t.)
3,000
1,000
300
5
2
1
Radiance (10^8) (p s^{-1} cm^{-2} sr^{-1})
b
Anti-CD47 (i.t.)
CD47–LLO (i.t.)
P = 0.0060
Radiance (p s^{-1} cm^{-2} sr^{-1})
10^{10}
10^9
10^8
10^7
10^6
10^5
16 20 24 28 32
Time (d)
c
Anti-CD47 (i.t.)
CD47–LLO (i.t.)
Probability of survival
100
50
0
0 20 40 60
Time (d)
P = 0.0031
d
Anti-CD47
CD47–LLO
CD8 PD-1
e
Anti-CD47
CD47–LLO
Percent $CD8^+PD-1^+$ (%)
P = 0.0104
100 80 60 40 20 0
f
Anti-CD47
CD47–LLO
PD-L1
g
P = 0.0367
Percent $PD-L1^+DAPI^+$ (%)
25 20 15 10 5 0
Anti-CD47
CD47–LLO
h
Anti-CD47 (i.p.)
CD47–LLO (i.p.)
3.0
12
+Anti-PD-1
Anti-CD47 (i.p.)
CD47–LLO (i.p.)
8.2
20
Thy1.2–APC
CD8–PE
10^1 10^2 10^3 10^4 10^5 10^6
i
Tumor $CD8^+$ T cells
40 30 20 10 0
P = 0.0016
P = 0.0040
Anti-CD47
CD47–LLO
Anti-CD47
CD47–LLO
+Anti-PD-1
k
Anti-CD47 (i.p.)
CD47–LLO (i.p.)
Anti-PD-1
Anti-CD47 (i.p.) + anti-PD-1
CD47–LLO (i.p.) + anti-PD-1
P = 0.0248
P = 0.0203
P = 0.0488
Radiance (p s^{-1} cm^{-2} sr^{-1})
10^9 10^8 10^7 10^6 10^5
16 20 24 28 32 36
Time (d)
l
Anti-CD47 (i.p.)
CD47–LLO (i.p.)
Anti-PD-1
Anti-CD47 (i.p.) + anti-PD-1
CD47–LLO (i.p.) + antiPD-1
Probability of survival
100
50
0
0 20 40 60 80
Time (d)
P = 0.0007
j
12 d
16 d
20 d
28 d
32 d
36 d
40 d
Anti-CD47 (i.p.)
CD47–LLO (i.p.)
Anti-PD-1
Anti-CD47 (i.p.) + anti-PD-1
CD47–LLO (i.p.) + anti-PD-1
3,000
1,000
300
5
2
1
Radiance (10^8) (p s^{-1} cm^{-2} sr^{-1})
m
Treatment naive
i.t., CD47–LLO, survivor
i.p., CD47–LLO, survivor
4T1 tumor volume (mm^3)
1,000 800 600 400 200 0
8 11 14 16 20 24 28
Time (d)
n
Long-term survivor of 4T1Br4 tumor rechallenge
Splenic $CD8^+$ cells
+Tumor cells
IFN-γ release
o
IFN-γ
EO771
4T1Br4
4T1Br4 naive
4T1Br4 survivor
p
4T1Br4 tumor naive
4T1Br4 survivor
Spots per well
80 60 40 20 0
P > 0.9999
P = 0.0458
EO771
EO771
4T1Br4
4T1Br4

Fig. 8 | CD47–LLO drives systemic anti-tumor immunity to inhibit breast cancer metastasis. a,**b**, Representative IVIS spectrum images (**a**) and quantified signal intensity (**b**) of Luc-4T1Br4 breast tumors before tumor debulking (that is, on day 12 after tumor inoculation) and after tumor debulking (that is, days 16–36). *n* = 7 for CD47–LLO and *n* = 7 for anti-CD47 antibody. **c**, Survival curves for each treatment group. **d**, Arrowheads show $CD8^+$ cells (red) co-labeled with anti-PD-1 antibody (green). Scale bar, 20 µm. **e**, Quantification of $CD8^+$ cells that co-labeled with anti-PD-1 (*n* = 3 biologically independent experiments). **f**, PD-L1 protein expression levels in frozen tissue tumor sections. Scale bar, 20 µm. **g**, Quantification of $DAPI^+$ cells that co-labeled with anti-PD-L1 (*n* = 3 biologically independent experiments). **h**,**i**, Flow cytometry analysis (**h**) and quantification (**i**) of $CD8^+$ T cells isolated from 4T1Br4 tumors treated with intraperitoneal (i.p.) CD47–LLO (*n* = 5), anti-CD47 antibody (*n* = 5), anti-CD47 plus anti-PD-1 antibody (*n* = 6) or CD47–LLO and anti-PD-1 antibody (*n* = 8). **j**,**k**, Representative IVIS spectrum images (**j**) and quantified signal intensity (**k**) of Luc-4T1Br4 breast tumors. *n* = 4 for intraperitoneal CD47–LLO, *n* = 7 for anti-CD47 antibody. For mice treated with anti-PD-1 antibody, *n* = 6 for anti-PD-1 antibody alone, *n* = 8 for anti-CD47 antibody and *n* = 6 for CD47–LLO. **l**, Survival curves for each treatment group. CD47-LLO, *n* = 5; anti-CD47 antibody, *n* = 7; anti-PD-1 antibody, *n* = 5; other treatment groups, *n* = 6. **m**, Tumor volumes were monitored for the indicated periods. *n* = 5 tumor-naive animals, *n* = 3 intratumoral CD47–LLO animals, *n* = 4 intraperitoneal CD47–LLO animals. **n**, Schematic illustrating the establishment of splenic $CD8^+$ T cell tumor co-cultures. **o**,**p**, IFN-γ ELISPOT assay, scale bar, 1 mm (**o**) and quantification (**p**). *n* = 3 biologically independent samples. Data shown represent mean ± s.e.m. (**b**,**e**,**g**,**k**,**m**) or mean ± s.d. (**i**,**p**) analyzed by two-sided unpaired Student's *t*-test (**e**,**g**,**p**), Welch analysis of variance with Dunnett's multiple-comparison test (**i**), two-way analysis of variance with the Benjamini, Krieger and Yekutieli multiple-comparison test (**b**,**k**) or two-sided log-rank (Mantel–Cox) test (**c**,**l**). Panel **n** created by modifying graphics from BioRender.com.

organs revealed no changes in tissue morphology, necrosis or inflammation after administration of CD47–LLO, either as monotherapy or in combination with anti-PD-1 antibody (Extended Data Fig. 10f). However, inflammatory cytokines including IL-6 and IL-1β were elevated in mouse serum in the hours after intraperitoneal CD47–LLO administration (Extended Data Fig. 10g,h). We also noted an increase in anti-LLO antibodies in the serum of some mice weeks after treatment completion (Extended Data Fig. 10i). These findings suggest that, although systemically delivered CD47–LLO synergizes with T cell checkpoint blockade, it also carries risks of systemic inflammation and an anti-drug antibody (ADA) response. Overall, CD47–LLO effectively sensitized poorly immunogenic tumors to PD-1 blockade, thereby providing a rationale for the use of CD47–LLO in combination with immune checkpoint inhibitors to generate systemic anti-tumor responses.

To verify the generation of tumor-specific memory in CD47–LLO-treated tumor-free animals, we rechallenged treatment-naive (unimmunized) mice and mice with long-term survival. Long-term survivors were found to be resistant to 4T1Br4 tumor cell rechallenge, suggesting that CD47–LLO produced anti-tumor memory responses (Fig. 8m). We collected T cells from the spleens of CD47–LLO-treated mice that survived 4T1Br4 tumor rechallenge and then rechallenged them with EO771 or 4T1Br4 cells in vitro (Fig. 8n). Only 4T1Br4 cells elicited a robust IFN-γ response (Fig. 8o,p). Together, these results provide compelling evidence that CD47–LLO enhances local and systemic immune activation to drive tumor-specific memory in vivo.

Discussion

The adoption of bacteria as nonspecific immune stimulants dates back over a century, when Coley toxins were found to retard the growth of malignant tumors[43]. LLO operates by permeabilizing cholesterol-rich phagolysosome membranes, facilitating the escape of *L. monocytogenes* into the cytosol[13–15]. This life cycle exposes *Listeria*-derived proteins to both MHC class II presentation after lysosomal degradation and MHC class I presentation after cytosolic release. These unique characteristics have led to investigations of *L. monocytogenes* as a delivery vector for antiviral and tumor antigens, including DNA vaccines with LLO fusion proteins and chemical conjugates combining LLO with external antigens[44–49]. These systems have been used to immunize against tumor challenge with varying degrees of success. However, LLO has not yet been exploited to enhance the cytosolic immune detection or presentation of engulfed tumor cargo. Based on its effects of increasing phagocytosis and the cytosolic delivery of tumor peptides and DNA, CD47–LLO demonstrates enhanced therapeutic effectiveness against a variety of solid tumors compared with anti-CD47 antibody alone and shows synergistic effects when combined with anti-PD-1 therapy. These results together support CD47–LLO's potential to join an expanding platform of ADCs that leverage immune-stimulating strategies, including TLR7 and TLR8 agonism[50], to enhance APC functionalities.

Intratumoral delivery of CD47–LLO produced a systemic anti-tumor response that bridged innate and adaptive immunity. Previous clinical trials employing bacterial toxins and immune agonists have identified nonspecific immune stimulation and dose frequency-dependent ADA titers as factors affecting drug tolerability, pharmacokinetics and systemic exposure[51,52]. We also detected signals of broader immune activation with systemic delivery of CD47–LLO. Cytokine levels in animal serum increased hours after intraperitoneal administration, and ADAs arose weeks after the animals completed treatment. Image-guided intratumoral injection of ADCs is being widely evaluated and, given these mentioned concerns, may be a better-suited administration route for CD47–LLO[53]. Future CD47–LLO derivatives, including conjugates with optimized anti-CD47 Fc domains[54], may further enhance its therapeutic efficacy and potential toxicity. The versatility of click chemistry-empowered protein–antibody assembly will also enable exploration of LLO conjugates with other phagocytosis checkpoint inhibitors[55]. These investigations will improve tumor targeting efficiency and toxin payload delivery and thereby advance ATCs for cancer immunotherapy applications.

Methods

Ethics statement

All mouse experiment protocols were reviewed and approved by the Institutional Animal Care and Use Committee of the University of Texas MD Anderson Cancer Center (00002163) and the University of Texas Southwestern Medical Center (2018-102602).

CD47–LLO and IgG–LLO antibody conjugation

The MIAP410 antibody (Bio X Cell, BE0283) was dialyzed against PBS buffer, pH 7.2. The dialyzed antibody was then modified with the click chemistry labeling reagent DBCO–PEG4–NHS ester (Conju-Probe, CP-2028) for 30 min at room temperature. Excess cross-linker was removed by dialysis against PBS buffer, pH 7.2. The buffer of LLO protein (GenScript) was exchanged for PBS buffer, pH 7.2 with a PD-10 column (GE Healthcare, 17085101), followed by modification with the click chemistry cross-linking reagent SPDP–PEG11–azide (BroadPharm, BP-25143). Excess click reagent was removed by buffer exchange, and then the modified LLO protein was mixed with antibody and allowed to react overnight at room temperature. Unconjugated antibody and LLO proteins were removed by affinity and size exclusion chromatographic methods, respectively. The coupling efficiency was determined by reducing 4–15% gradient SDS–PAGE, and the major products had a molar ratio (LLO protein/antibody) of ~1–2 to 1. The conjugate was concentrated to 2 mg ml^{-1} in PBS buffer, pH 7.2 and stored at 4 °C. Mouse IgG1 (Bio X Cell, BE0083) was conjugated to LLO by using similar methods.

Transmission electron microscopy

Samples with protein A Au-NPs (Nanocs, GP20-PA-1) were fixed with a solution containing 3% glutaraldehyde plus 2% paraformaldehyde in 0.1 M cacodylate buffer, pH 7.3 and then washed with 0.1 M sodium cacodylate buffer and treated with 0.1% Millipore-filtered cacodylate-buffered tannic acid, postfixed with 1% buffered osmium tetroxide and stained en bloc with 1% Millipore-filtered uranyl acetate. The samples were dehydrated with increasing concentrations of ethanol, infiltrated and embedded in LX-112 medium. The samples were polymerized in an oven at 60 °C for approximately 3 d. Ultrathin sections were cut in a Leica Ultracut microtome (Leica), placed on Formvar-coated single-slot copper grids, stained with uranyl acetate and lead citrate and examined in a JEM 1010 transmission electron microscope (JEOL) at an accelerating voltage of 80 kV. Digital images were obtained with an AMT Imaging System (Advanced Microscopy Techniques).

To quantify numbers of intact vacuoles within BMDMs, images were converted to grayscale and processed with Icy Software (version 3.0, Institut Pasteur, Quantitative Image Analysis Unit; http://www.icy.bioimageanalysis.org). Intact cytoplasmic vacuoles were detected and quantified per BMDM by using the HK-Means segmentation platform[27].

Mice

C57BL/6J, C57BL/6J-*Sting1*$^{\mathrm{gt}}$/J, BALB/cJ and OT-I (C57BL/6-Tg(TcraTcrb)-1100Mjb/J) rodents were procured from Jackson Laboratory and maintained at the animal facility of the University of Texas MD Anderson Cancer Center in a pathogen-free environment, with an ambient temperature of 22 °C and a humidity content of 50%. These mice were sustained on a regular diet and hydration schedule, under a cycle of 12 h of light followed by 12 h of darkness. For orthotopic breast cancer models, tumors were inoculated into the mammary fat pad of female rodents aged 6 to 8 weeks. For orthotopic melanoma models, tumors were inoculated into the right flank of male C57BL/6J mice aged 6 to 8 weeks. For the depletion of CD8$^+$ T cells, each rodent was given an intraperitoneal injection of 300 μg of anti-CD8 antibody, dispensed 24 h before other interventions (InVivoMAb, BE0117). Similarly, for the elimination of F4/80$^+$ cells, an intraperitoneal injection of 300 μg of anti-CSF1 antibody was given to each mouse, also 24 h in advance of further treatments (InVivoMAb, BE0213). These injections were replicated every 72 h until the end of the study. All procedures involving animals were authorized and performed according to the standards of the Institutional Animal Care and Use Committee of the University of Texas MD Anderson Cancer Center. In line with animal ethics guidelines, the mice were humanely euthanized when the tumor diameter reached 20 mm or when the animals displayed indicators of distress that aligned with the established institutional standards for initiating early euthanasia in all experiments of tumor inhibition. Signs for euthanasia include labored breathing, abnormal movement, hypothermia, hunched posture and more than 20% of body weight loss compared with baseline. Maximal tumor diameter was not exceeded in this study.

Cell cultures

The 4T1 mouse mammary carcinoma cell line was obtained from the American Type Culture Collection. The Luc-4T1Br4 variant, incorporating the red-shifted firefly luciferase (Red-FLuc) gene from *Luciola italica*, was measured for bioluminescence with an in vivo imaging system (IVIS) to evaluate luminescent intensity[56]. The EO771 mouse mammary carcinoma cell line was acquired from CH3 BioSystems. The mouse melanoma D4M3A cell line was a gift from D. Fisher (Massachusetts General Hospital). The mouse KPC cell line was a gift from D. Jiang (MD Anderson Cancer Center). Mouse BMDMs and BMDCs were isolated from the femoral bone marrow of the posterior limbs of C57BL/6J mice and established according to previous protocols. BMDMs were proliferated and activated with macrophage colony-stimulating factor (M-CSF, 50 ng ml^{-1}) by standardized methods. For BMDC differentiation, monocytes from bone marrow were differentiated in cell culture medium including granulocyte–macrophage colony-stimulating factor (GM-CSF, 20 ng ml^{-1}) and IL-4 (10 ng ml^{-1}) for 10 d. The authenticity of these cultivated cells was confirmed by flow cytometry, identifying BMDMs as CD45$^+$CD11b$^+$ and BMDCs as CD45$^+$CD11c$^+$MHC-II$^+$. The 4T1Br4, KPC, D4M.3A and EO771 cultures were propagated in RPMI 1640 medium, whereas BMDMs and BMDCs were propagated in DMEM medium. All growth media were supplemented with 10 mmol l^{-1} HEPES, 10% FBS, 1% sodium pyruvate, 100 U ml^{-1} penicillin G sodium and 100 μg ml^{-1} streptomycin sulfate. Cells were incubated at 37 °C in a humid atmosphere with a 5% CO$_2$ balance. All employed cell cultures were regularly examined and validated as free of *Mycoplasma* by biochemical testing with Hoechst staining. Flow cytometry gating strategies are shown in Supplementary Fig. 5.

Macrophage and dendritic cell phagocytosis assay

EO771 cells were labeled with CFSE dye according to the supplier's instructions (Invitrogen, C34554) and then seeded (1.5×10^5 cells per 12-well plate) overnight. Cells were treated with 2 μg ml^{-1} IgG, IgG–LLO, anti-CD47 antibody or CD47–LLO for 3 h before the addition of BMDMs or BMDCs (4.5×10^5 cells) and incubated at 37 °C or at 4 °C in the presence or absence of 0.02% sodium azide for 12 h. The combined cell populations were gathered and fixed with 4% paraformaldehyde. BMDMs were stained for CD11b, and BMDCs were stained for CD11c and MHC-II. Flow cytometry analysis was used to evaluate the phagocytosis of CFSE$^+$ EO771 cells by BMDMs and BMDCs.

T cell activation and proliferation

CD8$^+$ T cells were collected from the spleens of OT-I transgenic mice and isolated according to the manufacturer's guidelines (CD8a$^+$ T Cell Isolation Kit, mouse, Miltenyi Biotec). BMDMs co-cultured with cancer cells were treated with IgG, anti-CD47 antibody or CD47–LLO for 1 d before the addition of Far Red-stained OT-I cells. Cells were incubated for 3 d to allow T cell proliferation and activation. The cells were then isolated and stained with fluorophore-tagged antibodies and a cell viability dye. The Invitrogen CellTrace Far Red kit was used to monitor distinct generations of proliferating cells by dye dilution.

Confocal laser scanning microscopy for phagocytosis

To visualize phagocytosis, EO771 cells pre-stained with CFSE were seeded on confocal chamber slides (eight-chamber slide systems, Lab-Tek II), and then BMDMs stained with Far Red Cell Proliferation Dye (Invitrogen, C34572) were added to the chamber. The cells were incubated for 12 h in the presence of 2 μg ml^{-1} CD47–LLO, anti-CD47 antibody, IgG–LLO or IgG and then fixed with 4% paraformaldehyde solution. The chamber slides were mounted, and cell images were obtained by confocal microscopy (FV3000, Olympus).

Enzyme-linked immunosorbent assay for cytokines

For supernatant collection in vitro, EO771 cells were co-cultured with BMDMs and 2 μg ml^{-1} CD47–LLO, anti-CD47 antibody, IgG–LLO or IgG for 24 h. Cytokines were quantified with mouse ELISA kits according to the manufacturer's instructions: mouse TNF (ELISA MAX Deluxe Set Mouse TNF-α, BioLegend), mouse IFN-γ (ELISA MAX Deluxe Set Mouse IFN-γ, BioLegend), IL-6 (ELISA MAX Deluxe Set Mouse IL-6, BioLegend), mouse IL-1β (ELISA MAX Deluxe Set Mouse IL-1β, BioLegend).

Western blotting

Cells were lysed with RIPA Lysis and Extraction Buffer (Thermo Fisher) enriched with 1% protease inhibitor mixture (Thermo Fisher, 78429) in accordance with the manufacturer's guidelines. Protein isolates were acquired from the supernatants, and their concentrations were measured with a BCA protein assay. The extracts were then boiled for 10 min, and equal amounts from each sample were loaded onto 10% SDS–PAGE minigels for gel electrophoresis (80 V in the stacking gel and 120 V in the resolving gel). After electrophoresis, the proteins in the gels were transferred to polyvinylidene difluoride membranes (Bio-Rad) and blocked using a 5% milk solution for 1 h at room temperature.

These membranes were then incubated with primary antibodies at 4 °C overnight and subsequently with secondary antibodies according to the protocol provided by the manufacturer (p-STING (Ser366) pAb (PA5-105674, Thermo Fisher Scientific, dilution of 1:200), STING (D2P2F) rabbit mAb (13647, Cell Signaling Technology, dilution of 1:200), cGAS (D3O8O) rabbit mAb (31659, Cell Signaling Technology, dilution of 1:200). The protein signals were detected using X-ray film for band intensity analysis. β-actin (4967, Cell Signaling Technology, dilution of 1:500) was used as a benchmark for the loading control.

Real-time qPCR

RNA was isolated from cells by using TRIzol Reagent (Invitrogen) in accordance with the manufacturer's guidelines. For mRNA target identification, RNA strands were converted into complementary DNA using a cDNA Synthesis supermix kit (Bio-Rad). The synthesized cDNA was then amplified and assessed using real-time PCR supermix kits (Bio-Rad) with CFX Manager Software. The expression levels of each gene were calibrated against the expression of the gene encoding glyceraldehyde-3-phosphate dehydrogenase (GAPDH). Primers for mouse IFN and GAPDH genes were procured from Bio-Rad (mouse *Gapdh*, qMmuCED0027497; mouse *Ifna1*, qMmuCED0041680; mouse *Ifnb1*, qMmuCED0050444).

Tumor models

Orthotopic mammary fat pad tumors were established by injecting mouse breast cancer cells (EO771 in C57BL/6J mice for the primary tumor model, 4T1Br4 in BALB/cJ mice for the metastatic tumor model) at 1×10^6 cells in 50 µl PBS per mouse. Orthotopic melanoma models were established by injecting D4M.3A mouse cancer cells into the right flank at 1×10^6 cells in 50 µl PBS per mouse. Tumors were measured with calipers, and tumor volumes were calculated according to an ellipsoid formula ($1/2 \times \text{length} \times \text{width}^2$). Mice with 90–150-mm^3 tumors were randomly assigned into different treatment groups at 10 d (EO771 C57BL/6J tumor models, D4M.3A C57BL/6J tumor models) or 6 d (4T1 BALB/cJ tumor models) after tumor inoculation. For the EO771 C57BL/6J and D4M.3A C57BL/6J tumor models, 25 µg of IgG, anti-CD47, IgG–LLO, CD47–LLO and CD47–LLO-NC treatments were given intratumorally on days 10, 12 and 14. For the 4T1Br4 BALB/cJ animals receiving intratumoral injection, all groups were treated on days 7, 9 and 11. For the 4T1Br4 BALB/cJ animals given intraperitoneal injections, 100 µg of anti-CD47 antibody or CD47–LLO was given on days 8 and 10. The anti-PD-1 groups were given anti-PD-1 antibody (200 µg per mouse, InVivoMAb, BE0146) intraperitoneally on days 7, 9, 11, 14, 16 and 18.

In the metastasis model, primary 4T1Br4 tumors were surgically resected at day 13 after tumor inoculation to allow for the development of spontaneous metastases. Briefly, anesthetized mice were restrained on the operating table and given preemptive analgesia. A 3–4-mm incision was made around the tumor mass, exposing the skin covering the tumor and the mammary fat pad. Once the primary tumor was exposed, the tumor was carefully removed. Skin flaps were sutured closed. The mice were kept warm until recovery from anesthesia and were allowed to move around freely thereafter. Mice were imaged by bioluminescence to identify any residual tumor remaining after surgery.

For the tumor rechallenge experiments, mice that received intratumoral CD47–LLO and survived >80 d after 4T1Br4 inoculation were re-inoculated with 1×10^6 4T1Br4 cells. Mice that received intraperitoneal CD47–LLO and survived >80 d after 4T1Br4 inoculation were also re-inoculated with 1×10^6 4T1Br4 cells. Procedures in tumor growth experiments were consistent across all the tumor models.

Flow cytometry in vivo

Tumors and spleens were excised from tumor-bearing mice 1 or 2 d after the final treatment. Tumors were dissociated into single-cell suspensions by using a mouse tumor dissociation kit (Miltenyi Biotec). CD45$^+$ cells were enriched by using a CD45-positive selection method (CD45 MicroBeads, mouse, Miltenyi Biotec). Splenocytes were obtained by grinding the spleens and then lysing red blood cells. Both types of cells were stained with the corresponding antibodies for analysis by flow cytometry. Data were collected using BD Accuri C6 software version 227. Supplementary Table 1 provides information on antibody dilutions and amounts, company names, catalog numbers and clone numbers for all antibodies used in the study.

OVA tetramer assay

EO771-cOVA cells (1×10^6) were inoculated into the mammary pad of C57BL/6 mice. Intratumoral injections of CD47–LLO, anti-CD47 antibody, IgG–LLO and IgG were given to tumor-bearing mice from day 10 to day 14. Tumors collected on day 16 were dissociated, and tumor-infiltrating lymphocytes were isolated by the CD45$^+$ enrichment method described above. Cells were stained with Aqua cell viability dye, PE-Cy7 anti-CD45 antibody, APC anti-Thy1.2 antibody, PE anti-CD8 antibody and BV421 OVA tetramer (MBL) to verify OVA tetramer$^+$CD45$^+$ Thy1.2$^+$CD8$^+$ populations. Antibodies for surface staining were used at a 1:100 dilution and for intracellular staining at a 1:50 dilution.

Preparation of single-cell suspensions for scRNA-seq

Tumor tissues were prepared for single-cell fixed RNA profiling according to the manufacturer's instructions (10x Genomics, 1000414). Briefly, EO771 tumor-bearing C57BL/6 female mice were treated with 25 µg of IgG, anti-CD47 antibody or CD47–LLO via intratumoral injection on days 10, 12 and 14 after tumor inoculation. On day 16, mice were euthanized, and tumors were excised, cut into small pieces and digested for 10 min with collagenase D into a single-cell suspension according to the manufacturer's instructions (Roche Applied Science). Single-cell suspensions were filtered through a 30-µm strainer, labeled with Aqua and anti-CD45–PE antibody and fixed according to the manufacturer's instructions. Fluorescence-activated cell sorting was used to collect 100,000 Aqua-negative CD45–PE$^+$ cells per tumor. For scRNA-seq analysis, CD45$^+$ cells were pooled into three samples (CD47–LLO, anti-CD47 antibody and IgG), with $n = 4$ for CD47–LLO-treated tumors, $n = 4$ for anti-CD47-treated tumors and $n = 3$ for IgG-treated tumors.

scRNA-seq library preparation for 10x Genomics single-cell 3′ sequencing

Single-cell gene expression libraries for each of the three samples were prepared separately by following the protocols for Chromium Fixed RNA Profiling Reagent Kits for Multiplexed Samples (10x Genomics, User Guide, CG000527) To generate fixed RNA gene expression libraries, fixed single-cell suspensions were mixed with probes (PN-1000456) and hybridized overnight (16–24 h) at 42 °C. Cells with unique barcodes were pooled and mixed with the single-cell master mix, and the resulting cell suspensions were loaded on a 10x Chromium X system to capture. Gene expression libraries were generated by using a Single Cell Fixed RNA Hybridization & Library Kit (PN-1000415). All libraries were sequenced on an Illumina NovaSeq 6000 platform.

Single-cell RNA-seq analysis

Cell Ranger 7.1.0 (RRID:SCR_017344) was used to align the reads with the mouse reference genome GRCm39. For quality control, doublets were identified using Scrublet (RRID:SCR_018098) with a doublet score of >0.1, and cells were identified with number of features <200 and percentage of mitochondrial RNA >5. After the removal of low-quality data and doublets, single cells were normalized to the library size and $\log_2$ transformed by using Seurat version 4.3.0.1 (RRID:SCR_016341). Next, principal-component analyses based on the 2,000 most variably expressed genes was used for dimensional reduction. Principal components were used as input for Louvain-based graphing with a resolution of 0.2. Clustered-specific gene expression was used for cell annotation.

Gene set enrichment analysis

Differentially expressed genes were generated by using a fast Wilcoxon rank-sum test (presto package version 1.0.0, https://github.com/immunogenomics/presto). The gene list was used as input for the fgsea version 1.24.0 (RRID:SCR_020938) R package to identify enrichment of gene sets from the Kyoto Encyclopedia of Genes and Genomes (RRID:SCR_012773).

CellChat

CellChat version 1.6.1 (RRID:SCR_021946) and the CellChat mouse database of ligands and receptor pairs were used to identify changes in cell-to-cell communication patterns in CD47–LLO-treated tumors. We included ligands and receptors expressed in at least 10% of the population (default cutoff) and excluded any population with less than a minimum of 20 cells. CellChat then calculated the communication probability at the signaling pathway level, using a P-value threshold of 0.5 to determine significant interactions. Finally, plots were generated by using the built-in functions within CellChat and significant communications identified between cell types.

Immunohistochemical analysis

Tumor tissues were embedded in OCT, frozen, cryosectioned into 20-µm slices and mounted on slides. Slides were fixed, washed with TBS-T and blocked in TBS-T containing 3% BSA and 10% goat serum for 1 h. Slides were incubated with primary antibodies overnight and then washed and stained with appropriate secondary antibodies. Slides were then washed, mounted with coverslips, and analyzed by confocal or wide-field microscopy. To quantify numbers of immune cell populations within tumors, images were converted to grayscale and processed with Icy Software (version 3.0; Institut Pasteur, Quantitative Image Analysis Unit; http://www.icy.bioimageanalysis.org). Individual fluorescent cell populations were detected and quantified per field of view by using the HK-Means segmentation platform[27].

To measure p-STING fluorescence intensity within F4/80$^+$ tumors, p-STING fluorescence (mean intensity of signal) was detected by using the ROI Statistics plugin from Icy Bioimaging Software. Individual F4/80$^+$ cells were identified with the HK-Means segmentation platform.

Hematoxylin and eosin staining

Paraffin sections were prepared by fixing tissue samples in 4% formalin for >24 h. After fixation, the samples were dehydrated with graded ethanol solutions and embedded in paraffin blocks. Sections of 4–5 µm in thickness were cut from the paraffin blocks by using a microtome and mounted onto glass slides. The sections were subsequently deparaffinized and rehydrated for staining with hematoxylin and eosin to visualize the cellular and tissue structures. The deparaffinized sections were incubated in a hematoxylin solution to stain the nuclei, followed by a brief rinse in running water. Next, the sections were differentiated in acid alcohol to remove excess hematoxylin, rinsed and counterstained with an eosin solution to highlight the cytoplasm and extracellular components. The stained sections were dehydrated with ethanol, cleared with xylene and mounted with a coverslip with mounting medium.

Anti-drug antibody assay

Recombinant LLO protein (40 µg ml^{-1}) was coated onto assay plates (MSD, L15XA-3) at 4 °C overnight. The next day, the plates were blocked with blocking buffer (MSD, R93AA-1) at room temperature for 1 h. The positive control antibody (anti-listeriolysin antibody, Abcam ab200538) and the mouse serum were diluted in blocking buffer and added to the plate. After a 1-h incubation at room temperature, plates were washed three times with PBS containing 0.05% Tween. The sulfo-tag secondary antibodies (MSD, R32AC-1 and R32AB-1) were diluted to 1:500 in blocking buffer and incubated with the plates for 1 h at room temperature. After three washes with PBS containing 0.05% Tween, read buffer (MSD, R92TC-2) was added and the plates were read with a MESO SECTOR S 600MM reader. The concentration of anti-LLO antibody in each serum sample was calculated based on the linear regressed standard curve generated by the positive control antibody.

Biodistribution assays

CD47–LLO and IgG1 (Bio X Cell, BE0083) were labeled with IR800CW–NHS ester (LI-COR) and conjugated according to the manufacturer's protocol. Briefly, IR800CW-tagged CD47–LLO or IgG1 was intratumorally or intraperitoneally injected into EO771 tumor-bearing mice. For biodistribution studies, IVIS images were obtained at predetermined time points. At 24 h after intratumoral injection or at 36 h after intraperitoneal injection, the mice were euthanized, organs and tumors were collected and then IVIS was used to quantify the fluorescence signals. Data were collected using Living Image Software 4.7.

Apoptosis assay

EO771, 4T1Br4, KPC, D4M.3A (at 2×10^5 cells per 12-well plate) and BMDMs (at 5×10^5 cells per 12-well plate) were treated with CD47–LLO or LLO for 24 h, as described in the main text. The cells were stained with FITC–annexin V and PI according to the manufacturer's protocol (Dead Cell Apoptosis Kits with Annexin V for Flow Cytometry, Thermo Fisher Scientific). Apoptotic events were measured by flow cytometry.

Evaluation of systemic toxicity

Six-week-old female C57BL/6J mice were intraperitoneally injected with CD47–LLO and anti-PD-1 antibody, CD47–LLO, anti-CD47 antibody or IgG. The body weights of the mice in each group were measured on days 2 and 9 after injection. On day 9, blood samples were collected from each mouse via cardiac puncture, and alanine aminotransferase (ALT), aspartate aminotransferase (AST), blood urea nitrogen and creatinine levels were evaluated from blood plasma and blood cells were used to assess the population of leukocytes. To measure serum cytokine levels following CD47–LLO treatment, serum from 6-week-old female C57BL/6J mice was collected 4 h following intraperitoneal injection. In a separate cohort of animals, organs including heart, liver, spleen, kidney and lungs were collected 2 d after intraperitoneal injection and stained with hematoxylin and eosin to determine toxicity via histologic analysis.

Hemolysis assay

Red blood cells were obtained by centrifuging blood samples from C57BL/6 mice and then treated with PBS, CD47–LLO or 10% Triton X-100 for 2 h at 37 °C. The red blood cells were then centrifuged to collect supernatant. The absorbance (A) at 540 nm of each sample was detected with a multireader. Hemolysis was calculated as hemolysis (%) = $(A_{\text{sample}} - A_{\text{PBS}})/(A_{\text{Triton X}} - 100 - A_{\text{PBS}}) \times 100$ (%).

Statistics and reproducibility

Data distribution was assumed to be normal, but this was not formally tested. No effect size was predetermined. No statistical method was used to predetermine sample size. Group sizes for in vivo experiments were determined empirically based on prior results of intragroup variability in tumor growth upon similar treatments. For in vitro experiments, group sizes were selected based on previous publications and prior knowledge of variation and were replicated at least three times in accordance with previously published studies[56,57]. For mouse tumor treatment experiments, mice that spontaneously rejected tumors were excluded from randomization and treatment. No other data were excluded. All experiments were repeated biologically, and all results were reproducible. In mouse tumor treatment experiments, mice were randomized to different treatment groups when the tumor reached a certain size (as described in the Methods). The investigators were not blinded to allocation during experiments and outcome assessment.

Reporting summary

Further information on research design is available in the Nature Portfolio Reporting Summary linked to this article.

Data availability

Data supporting the findings of this study are available within the article and its Supplementary Information. The sequencing data have been deposited in the National Center for Biotechnology Information Gene Expression Omnibus database under the publicly available accession number GSE255937. The GRCm39-based mouse reference genome is available from the UCSC Genome Browser (http://genome.ucsc.edu). Source data are provided with this paper.

References

1. Drago, J. Z., Modi, S. & Chandarlapaty, S. Unlocking the potential of antibody–drug conjugates for cancer therapy. *Nat. Rev. Clin. Oncol.* **18**, 327–344 (2021).
2. Martiniova, L., Zielinski, R. J., Lin, M., DePalatis, L. & Ravizzini, G. C. The role of radiolabeled monoclonal antibodies in cancer imaging and ADC treatment. *Cancer J.* **28**, 446–453 (2022).
3. Ackerman, S. E. et al. Immune-stimulating antibody conjugates elicit robust myeloid activation and durable antitumor immunity. *Nat. Cancer* **2**, 18–33 (2021).
4. Shastry, M. et al. Rise of antibody–drug conjugates: the present and future. *Am. Soc. Clin. Oncol. Educ. Book* **43**, e390094 (2023).
5. Motwani, M., Pesiridis, S. & Fitzgerald, K. A. DNA sensing by the cGAS–STING pathway in health and disease. *Nat. Rev. Genet.* **20**, 657–674 (2019).
6. Jiang, M. et al. cGAS–STING, an important pathway in cancer immunotherapy. *J. Hematol. Oncol.* **13**, 81 (2020).
7. Zhu, Y. et al. STING: a master regulator in the cancer–immunity cycle. *Mol. Cancer* **18**, 152 (2019).
8. Amouzegar, A., Chelvanambi, M., Filderman, J. N., Storkus, W. J. & Luke, J. J. STING agonists as cancer therapeutics. *Cancers* **13**, 2695 (2021).
9. Meric-Bernstam, F. et al. Phase I dose-escalation trial of MIW815 (ADU-S100), an intratumoral STING agonist, in patients with advanced/metastatic solid tumors or lymphomas. *Clin. Cancer Res.* **28**, 677–688 (2022).
10. Harrington, K. J. et al. Preliminary results of the first-in-human (FIH) study of MK-1454, an agonist of stimulator of interferon genes (STING), as monotherapy or in combination with pembrolizumab (pembro) in patients with advanced solid tumors or lymphomas. *Ann. Oncol.* **29**, 8, VIII712 (2018).
11. Janku, F. et al. Intratumoral injection of SYNB1891, a synthetic biotic designed to activate the innate immune system, demonstrates target engagement in humans including intratumoral STING activation. In *Proceedings of the American Association for Cancer Research Annual Meeting* CT110 (AACR, 2021).
12. Xu, M. M. et al. Dendritic cells but not macrophages sense tumor mitochondrial DNA for cross-priming through signal regulatory protein α signaling. *Immunity* **47**, 363–373 (2017).
13. Lee, H. J., Woo, Y., Hahn, T. W., Jung, Y. M. & Jung, Y. J. Formation and maturation of the phagosome: a key mechanism in innate immunity against intracellular bacterial infection. *Microorganisms* **8**, 1298 (2020).
14. Nguyen, B. N., Peterson, B. N. & Portnoy, D. A. Listeriolysin O: a phagosome-specific cytolysin revisited. *Cell. Microbiol.* **21**, e12988 (2019).
15. Podobnik, M. et al. Plasticity of listeriolysin O pores and its regulation by pH and unique histidine [corrected]. *Sci. Rep.* **5**, 9623 (2015).
16. Bavdek, A. et al. pH dependence of listeriolysin O aggregation and pore-forming ability. *FEBS J.* **279**, 126–141 (2012).
17. Köster, S. et al. Crystal structure of listeriolysin O reveals molecular details of oligomerization and pore formation. *Nat. Commun.* **5**, 3690 (2014).
18. Anand, P. K. et al. TLR2 and RIP2 pathways mediate autophagy of *Listeria monocytogenes* via extracellular signal-regulated kinase (ERK) activation. *J. Biol. Chem.* **286**, 42981–42991 (2011).
19. Chávez-Arroyo, A. & Portnoy, D. A. Why is *Listeria monocytogenes* such a potent inducer of CD8$^+$ T-cells? *Cell. Microbiol.* **22**, e13175 (2020).
20. Hansen, K. et al. *Listeria monocytogenes* induces IFNβ expression through an IFI16-, cGAS- and STING-dependent pathway. *EMBO J.* **33**, 1654–1666 (2014).
21. Chen, C. et al. The listeriolysin O PEST-like sequence co-opts AP-2-mediated endocytosis to prevent plasma membrane damage during *Listeria* infection. *Cell Host Microbe* **23**, 786–795 (2018).
22. Repp, H. et al. Listeriolysin of *Listeria monocytogenes* forms Ca^{2+}-permeable pores leading to intracellular Ca^{2+} oscillations. *Cell. Microbiol.* **4**, 483–491 (2002).
23. Vadia, S. et al. The pore-forming toxin listeriolysin O mediates a novel entry pathway of *L. monocytogenes* into human hepatocytes. *PLoS Pathog.* **7**, e1002356 (2011).
24. Xiao, L., Wang, Q. & Peng, H. Tumor-associated macrophages: new insights on their metabolic regulation and their influence in cancer immunotherapy. *Front. Immunol.* **14**, 1157291 (2023).
25. Plaza-Ga, I. et al. pH-triggered endosomal escape of pore-forming listeriolysin O toxin-coated gold nanoparticles. *J. Nanobiotechnology* **17**, 108 (2019).
26. Mulvihill, E., van Pee, K., Mari, S. A., Müller, D. J. & Yildiz, Ö. Directly observing the lipid-dependent self-assembly and pore-forming mechanism of the cytolytic toxin listeriolysin O. *Nano Lett.* **15**, 6965–6973 (2015).
27. Dufour, A. et al. Automated quantification of cell endocytosis using active contours and wavelets. In *2008 19th International Conference on Pattern Recognition* (IEEE, 2008).
28. de Chaumont, F. et al. Icy: an open bioimage informatics platform for extended reproducible research. *Nat. Methods* **9**, 690–696 (2012).
29. Dersh, D., Yewdell, J. W. & Wei, J. A SIINFEKL-based system to measure MHC class I antigen presentation efficiency and kinetics. *Methods Mol. Biol.* **1988**, 109–122 (2019).
30. Porgador, A., Yewdell, J. W., Deng, Y., Bennink, J. R. & Germain, R. N. Localization, quantitation, and in situ detection of specific peptide–MHC class I complexes using a monoclonal antibody. *Immunity* **6**, 715–726 (1997).
31. Jenkins, M. H. et al. Multiple murine BRaf^{V600E} melanoma cell lines with sensitivity to PLX4032. *Pigment Cell Melanoma Res.* **27**, 495–501 (2014).
32. Abdelfattah, N. et al. Single-cell analysis of human glioma and immune cells identifies S100A4 as an immunotherapy target. *Nat. Commun.* **13**, 767 (2022).
33. Benguigui, M. et al. Interferon-stimulated neutrophils as a predictor of immunotherapy response. *Cancer Cell* **42**, 253–265 (2023).
34. Gungabeesoon, J. A neutrophil response linked to tumor control in immunotherapy. *Cell* **186**, 1448–1464 (2023).
35. Hirschhorn, D. et al. T cell immunotherapies engage neutrophils to eliminate tumor antigen escape variants. *Cell* **186**, 1432–1447 (2023).
36. Ma, R. Y. et al. Macrophage diversity in cancer revisited in the era of single-cell omics. *Trends Immunol.* **43**, 546–563 (2022).
37. Stables, M. J. et al. Transcriptomic analyses of murine resolution-phase macrophages. *Blood* **118**, 192–208 (2011).
38. Espinosa-Carrasco, G. et al. Intratumoral immune triads are required for immunotherapy-mediated elimination of solid tumors. *Cancer Cell* **42**, 1202–1216 (2024).

39. Magen, A. et al. Intratumoral dendritic cell–CD4$^+$ T helper cell niches enable CD8$^+$ T cell differentiation following PD-1 blockade in hepatocellular carcinoma. *Nat. Med.* **29**, 1389–1399 (2023).
40. Andreatta, M. et al. Interpretation of T cell states from single-cell transcriptomics data using reference atlases. *Nat. Commun.* **12**, 2965 (2021).
41. Jin, S. et al. Inference and analysis of cell–cell communication using CellChat. *Nat. Commun.* **12**, 1088 (2021).
42. Alvarez-Martinez, M. et al. Blimp-1 and c-Maf regulate immune gene networks to protect against distinct pathways of pathobiont-induced colitis. *Nat. Immunol.* **25**, 886–901 (2024).
43. McCarthy, E. F. The toxins of William B. Coley and the treatment of bone and soft-tissue sarcomas. *Iowa Orthop. J.* **26**, 154–158 (2006).
44. Mason, N. J. et al. Immunotherapy with a HER2-targeting *Listeria* induces HER2-specific immunity and demonstrates potential therapeutic effects in a phase I trial in canine osteosarcoma. *Clin. Cancer Res.* **22**, 4380–4390 (2016).
45. Neeson, P., Pan, Z. K. & Paterson, Y. Listeriolysin O is an improved protein carrier for lymphoma immunoglobulin idiotype and provides systemic protection against 38C13 lymphoma. *Cancer Immunol. Immunother.* **57**, 493–505 (2008).
46. Paterson, Y., Guirnalda, P. D. & Wood, L. M. *Listeria* and *Salmonella* bacterial vectors of tumor-associated antigens for cancer immunotherapy. *Semin. Immunol.* **22**, 183–189 (2010).
47. Sewell, D. A. et al. Recombinant *Listeria* vaccines containing PEST sequences are potent immune adjuvants for the tumor-associated antigen human papillomavirus-16 E7. *Cancer Res.* **64**, 8821–8825 (2004).
48. Singh, R., Dominiecki, M. E., Jaffee, E. M. & Paterson, Y. Fusion to listeriolysin O and delivery by *Listeria monocytogenes* enhances the immunogenicity of HER-2/neu and reveals subdominant epitopes in the FVB/N mouse. *J. Immunol.* **175**, 3663–3673 (2005).
49. Witte, C. E. et al. Innate immune pathways triggered by *Listeria monocytogenes* and their role in the induction of cell-mediated immunity. *Adv. Immunol.* **113**, 135–156 (2012).
50. Li, B. T. et al. A phase 1/2 study of a first-in-human immune-stimulating antibody conjugate (ISAC) BDC-1001 in patients with advanced HER2-expressing solid tumors. *J. Clin. Oncol.* **41**, 2538 (2023).
51. US FDA. *NDA/BLA Multi-Disciplinary Review and Evaluation BLA 761104, Lumoxiti, Moxetumomab Pasudotox* www.accessdata.fda.gov/drugsatfda_docs/nda/2018/761104Orig1s000MultidisciplineR.pdf (2018).
52. Janku, F. et al. Preclinical characterization and phase I study of an anti-HER2–TLR7 immune-stimulator antibody conjugate in patients with HER2$^+$ malignancies. *Cancer Immunol. Res.* **10**, 1441–1461 (2022).
53. Chang, H.-P. et al. Pharmacokinetics and pharmacodynamics of antibody–drug conjugates administered via subcutaneous and intratumoral routes. *Pharmaceutics* **15**, 1132 (2023).
54. Osorio, J. C. et al. The antitumor activities of anti-CD47 antibodies require Fc–FcγR interactions. *Cancer Cell* **11**, 2051–2065 (2023).
55. Bradley, C. A. CD24 — a novel 'don't eat me' signal. *Nat. Rev. Cancer* **19**, 541 (2019).
56. Lu, Y. et al. Immunological conversion of solid tumours using a bispecific nanobioconjugate for cancer immunotherapy. *Nat. Nanotechnol.* **17**, 1332–1341 (2022).
57. Li, X. et al. Cancer immunotherapy based on image-guided STING activation by nucleotide nanocomplex-decorated ultrasound microbubbles. *Nat. Nanotechnol.* **17**, 891–899 (2022).

Acknowledgements

We thank K. Duprez and F. Han (Structure Based Design, Inc.) and Bio-Synthesis, Inc. for expertise with protein–antibody conjugation, K. Dunner, Jr (High Resolution Electron Microscopy Facility) for help with transmission electron microscopy image acquisition, D. Fisher (Massachusetts General Hospital) for the gift of the D4M.3A melanoma cell line, J. Zhang of MD Anderson's Department of Experimental Radiation Oncology for processing histologic samples; V. Van and K. L. Maldonado at MD Anderson's Small Animal Imaging Facility for helping with the animal experiments, N. R. Vaughn and N. Nguyen at MD Anderson's Flow Cytometry and Cellular Imaging Core Facility for helping with flow cytometry experiments, C. Shi and J. Yan at MD Anderson's Oncology Research for Biologics and Immunotherapy Translation platform for helping with ADA experiments and C. Wogan from MD Anderson's Division of Radiation Oncology for editorial help. This work was supported in part by the National Institutes of Health (R01NS117828 to W.J.) and the American Cancer Society (RSG-22-052-01-IBCD to W.J.), the Radiological Society of North America Resident Grant (to B.R.S.), the SITC Merck Cancer Immunotherapy Clinical Fellowship (to B.R.S.), the American Society of Clinical Oncology Young Investigator Award (to B.R.S.), the American Cancer Society award (PF-24-1156745-01-ET, grant https://doi.org/10.53354/ACS.PF-24-1156745-01-ET.pc.gr.193703 (to B.R.S.)), the Susan G. Komen Foundation Career Transition Award (to Y.W.) and the ABTA and Uncle Kory Foundation Fellowship (to K.H.).

Author contributions

W.J., B.Y.S.K., B.R.S. and Y.W. conceived the project and were responsible for all phases of the research. B.R.S. conducted the majority of the experiments and data analyses. Y.W., A.W., N.T., D.L., J.E., K.H., S.D., J.H., Y.M., A.G., S.D.J., M.C., M.K., T.D.G., A.C.K., J.L. and A.A. assisted with data collection and interpretation. N.T. and K.Y. performed bioinformatics analysis. The manuscript was drafted by B.R.S., B.Y.S.K. and W.J. and was revised and approved by all authors.

Competing interests

A provisional patent application based on the technology described in the paper has been filed by the Board of Regents, the University of Texas System, with W.J., B.R.S., Y.W. and B.Y.S.K. as inventors. The other authors declare no competing interests.

Additional information

Extended data is available for this paper at https://doi.org/10.1038/s43018-025-00919-0.

Supplementary information The online version contains supplementary material available at https://doi.org/10.1038/s43018-025-00919-0.

Correspondence and requests for materials should be addressed to Betty Y. S. Kim or Wen Jiang.

Peer review information *Nature Cancer* thanks Dennis Discher and the other, anonymous, reviewer(s) for their contribution to the peer review of this work.

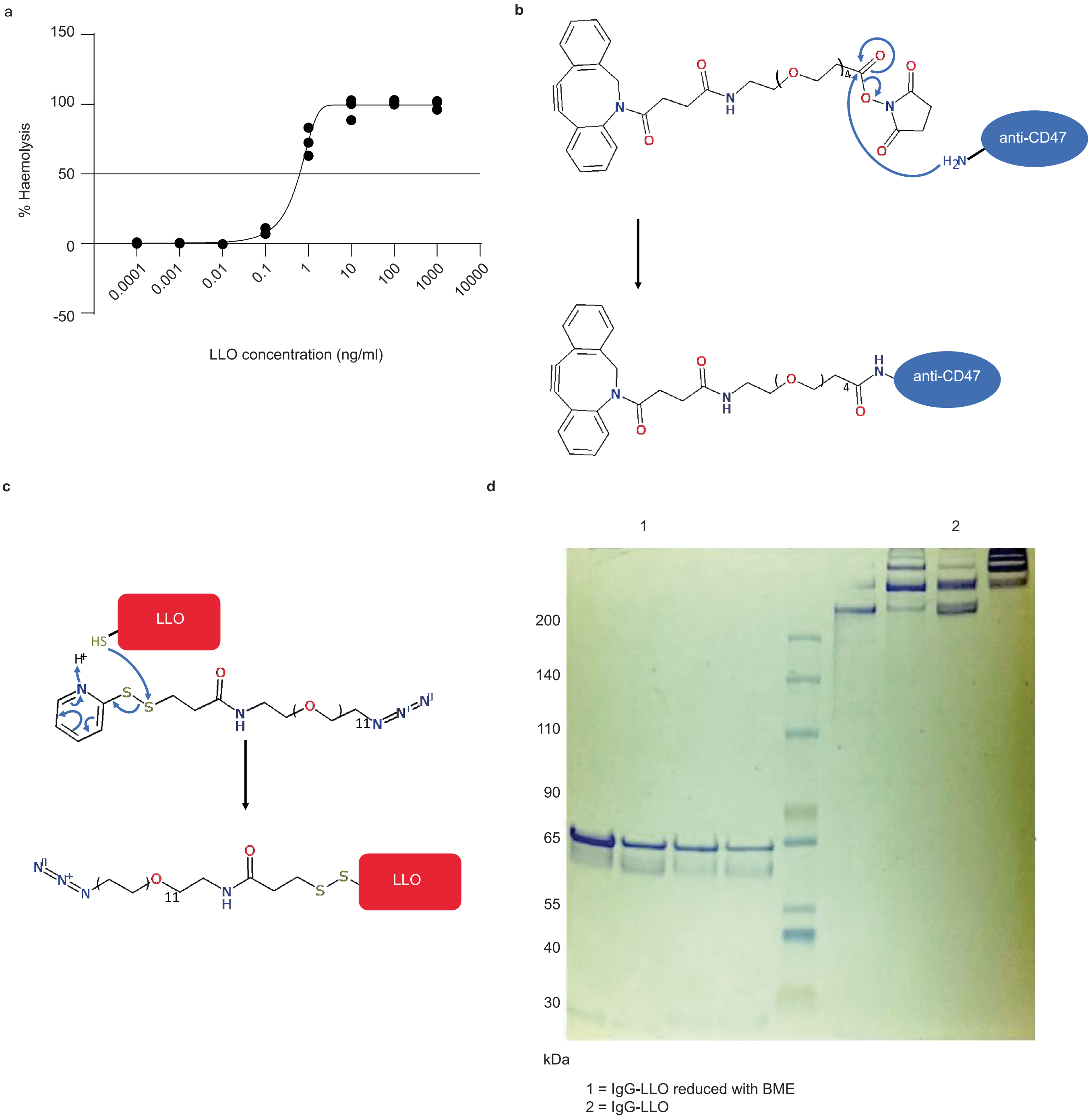

Extended Data Fig. 1 | Conjugation of anti-CD47 and IgG1 to Listeriolysin O. **a**, Results of sheep red blood cell (sRBC) haemolysis assay of purified LLO. Data show *n* = 3 biologically independent experiments. **b**, The MIAP410 antibody (BioXCell, Cat#BE0283) or the IgG1 antibody (BioXCell, Cat#BE0083) was dialyzed against phosphate-buffered saline (PBS) buffer, pH 7.2, and the dialyzed antibody was then modified with the click chemistry labelling reagent DBCO-PEG4-NHS ester (Conju-Probe, SKU# CP-2028) for 30 min at room temperature. The crosslinker in excess was removed by dialysis against PBS buffer, pH 7.2. **c**, The buffer of Listeriolysin O protein (Genscript) was exchanged with PBS buffer, pH 7.2, by PD-10 column (GE healthcare, Cat# 17085101), followed by modification with the click chemistry crosslinking reagent SPDP-PEG11-azide (BroadPharm, Cat# BP-25143). **d**, SDS-PAGE results of IgG-LLO conjugate in reductive and non-reductive loading buffers. Representative gel of *n* = 4 biological replicates shown.

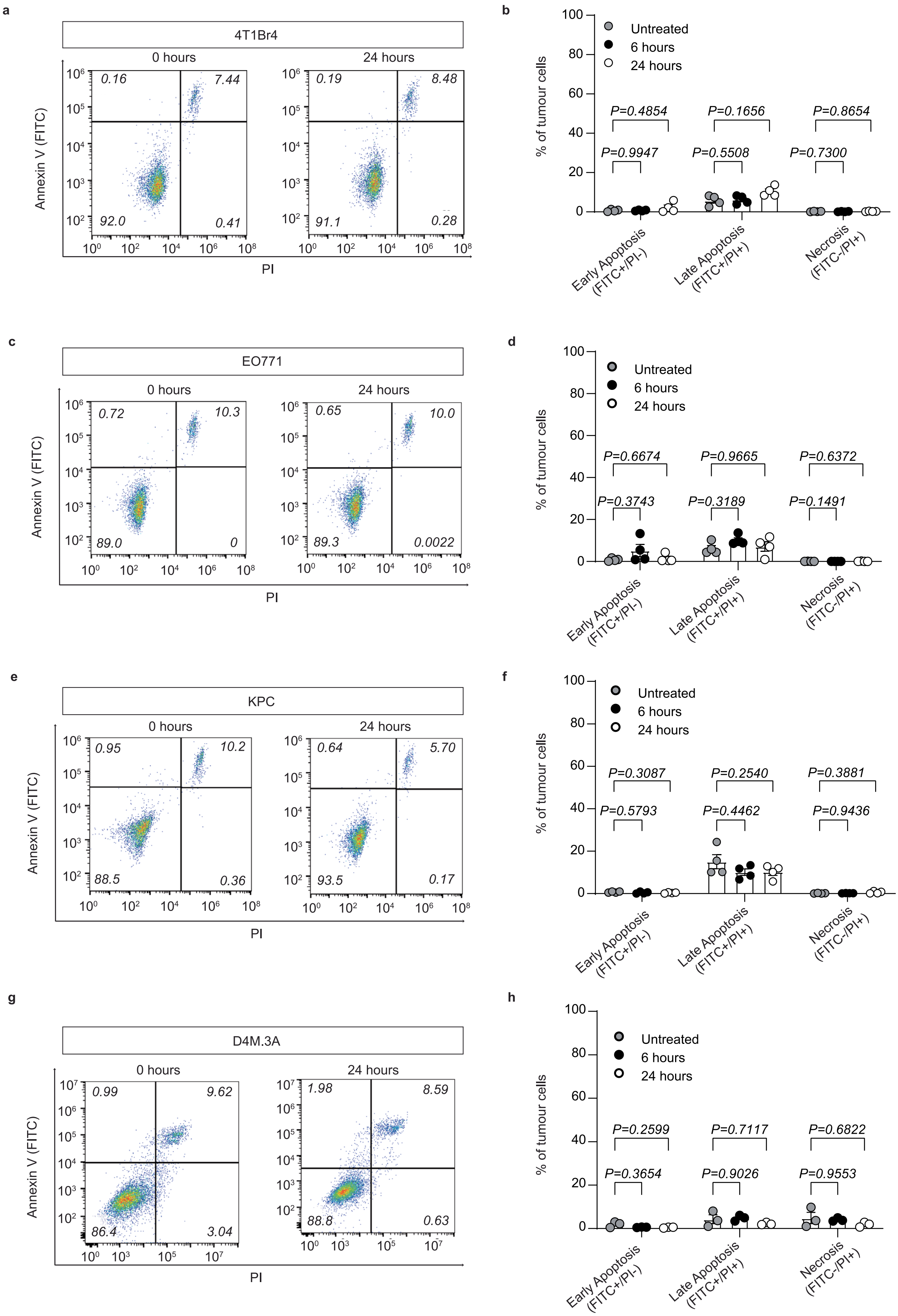

Extended Data Fig. 2 | *In vitro* toxicity assays of CD47-LLO with cancer cell lines. a-h, Flow cytometry analysis and quantification of apoptosis and necrosis in 4T1Br4 (**a-b**), EO771 (**c-d**), KPC (**e-f**), and D4M.3 A (**g-h**) cells after treatment with 2 µg/mL CD47-LLO for 0, 6, or 24 hours (*n* = 4 biologically independent experiments for **b**, **d**, **f**, and *n* = 3 for **h**). Data shown represent mean ± s.d. (**b**, **d**, **f**, **h**) analyzed by one-way analysis of variance with Tukey's multiple comparisons test.

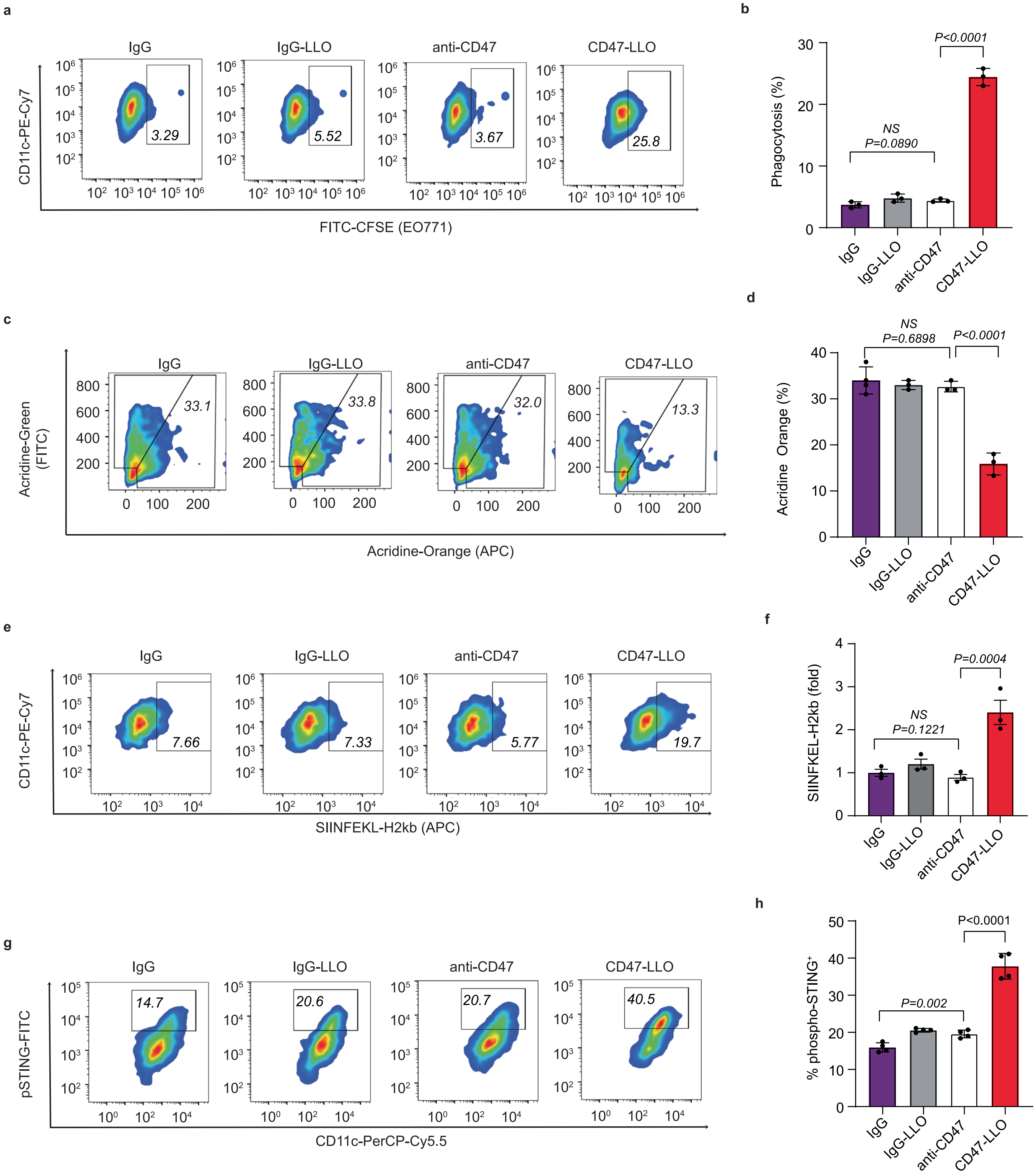

Extended Data Fig. 3 | CD47-LLO promotes dendritic cell phagocytosis, lysosomal permeabilization, antigen presentation, and cGAS-STING activation *in vitro*. **a**, Flow cytometry analysis and **b**, quantification of phagocytic activity of bone marrow-derived dendritic cells (BMDCs) as evaluated by flow cytometry. BMDCs were collected from n = 3 C57BL6 mice. **c**, Flow cytometry analysis and **d**, quantification of BMDCs stained with acridine orange. BMDCs were collected from n = 4 C57BL6 mice for IgG treatment and n = 3 for remaining treatment groups. **e**, Flow cytometry analysis and **f**, quantification of cross-presentation of SIINFEKL–H2Kb peptides on the surfaces of BMDCs (n = 3). **g**, Flow cytometry analysis and **h**, quantification of pSTING levels in BMDCs isolated from co-cultures with EO771 cells. n = 4 C57BL6 mice. Data shown represent mean ± s.d. (**b, d, f, h**) analyzed by one-way analysis of variance with Tukey's multiple comparisons test.

https://doi.org/10.1038/s43018-025-00919-0

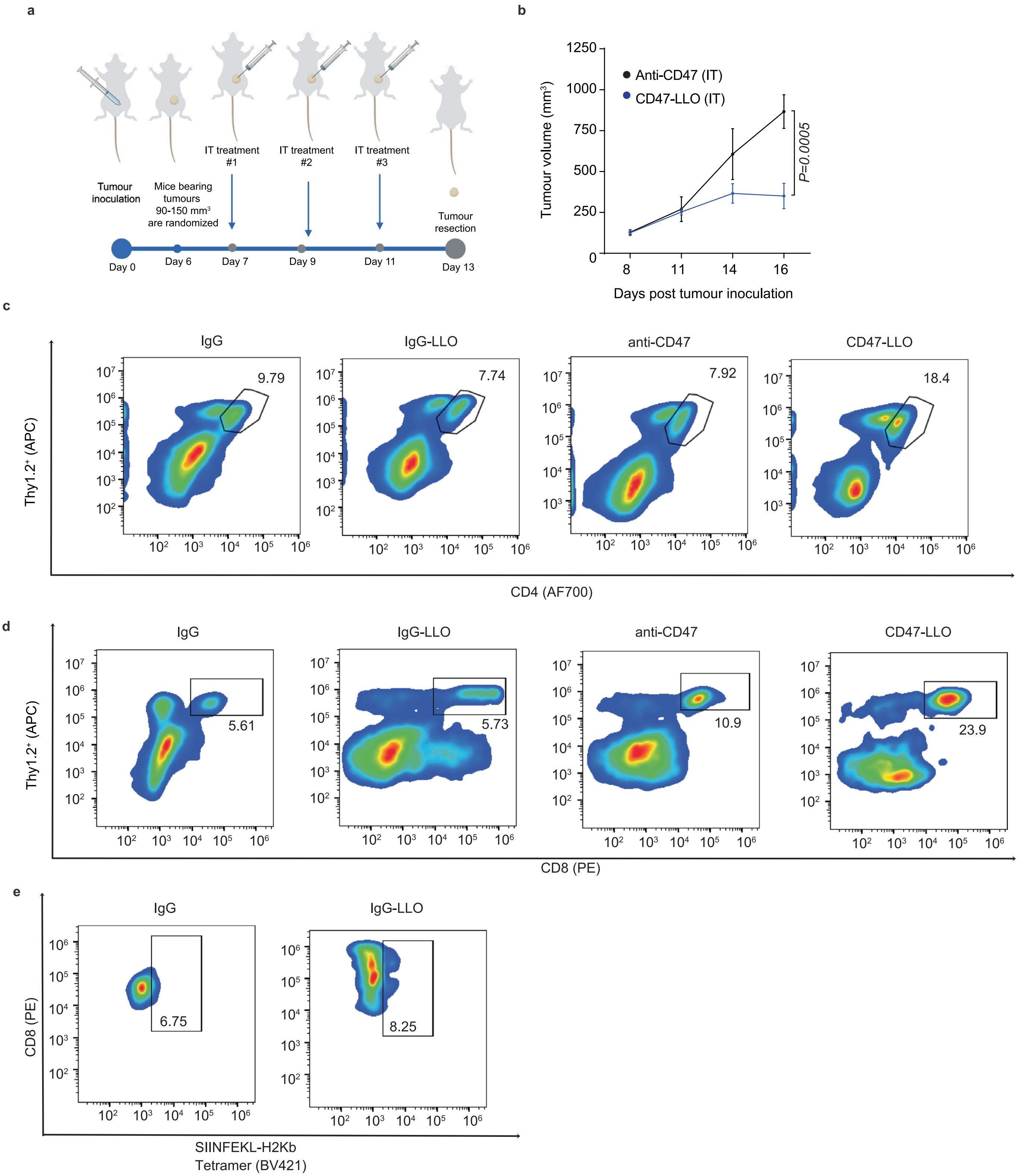

Extended Data Fig. 4 | Antitumour effect of intratumoural CD47-LLO in 4T1Br4 and EO771 models. a, Schematic of experiments involving intratumoural (IT) injections of CD47-LLO or anti-CD47 in syngeneic orthotopic 4T1Br4 breast cancer models. **b**, 4T1Br4 tumour volumes after IT injection of anti-CD47 or CD47-LLO. *n* = *4* for intratumoural CD47-LLO, *n* = *4* for intratumoural anti-CD47. **c-d**, Flow cytometry analysis of $CD4^+$ (**c**) and $CD8^+$ (**d**) tumour-associated lymphocytes in EO771 tumours at day 16 after tumour inoculation in each group. **e**, Flow cytometry analysis of SIINFEKL–H2Kb $tetramer^+CD8^+$ T cells within the tumour microenvironment. Data shown represent mean ± s.e.m. (**b**) analyzed by two-way analysis of variance with Tukey's multiple comparisons test. Panel **a** created by modifying graphics from BioRender.com.

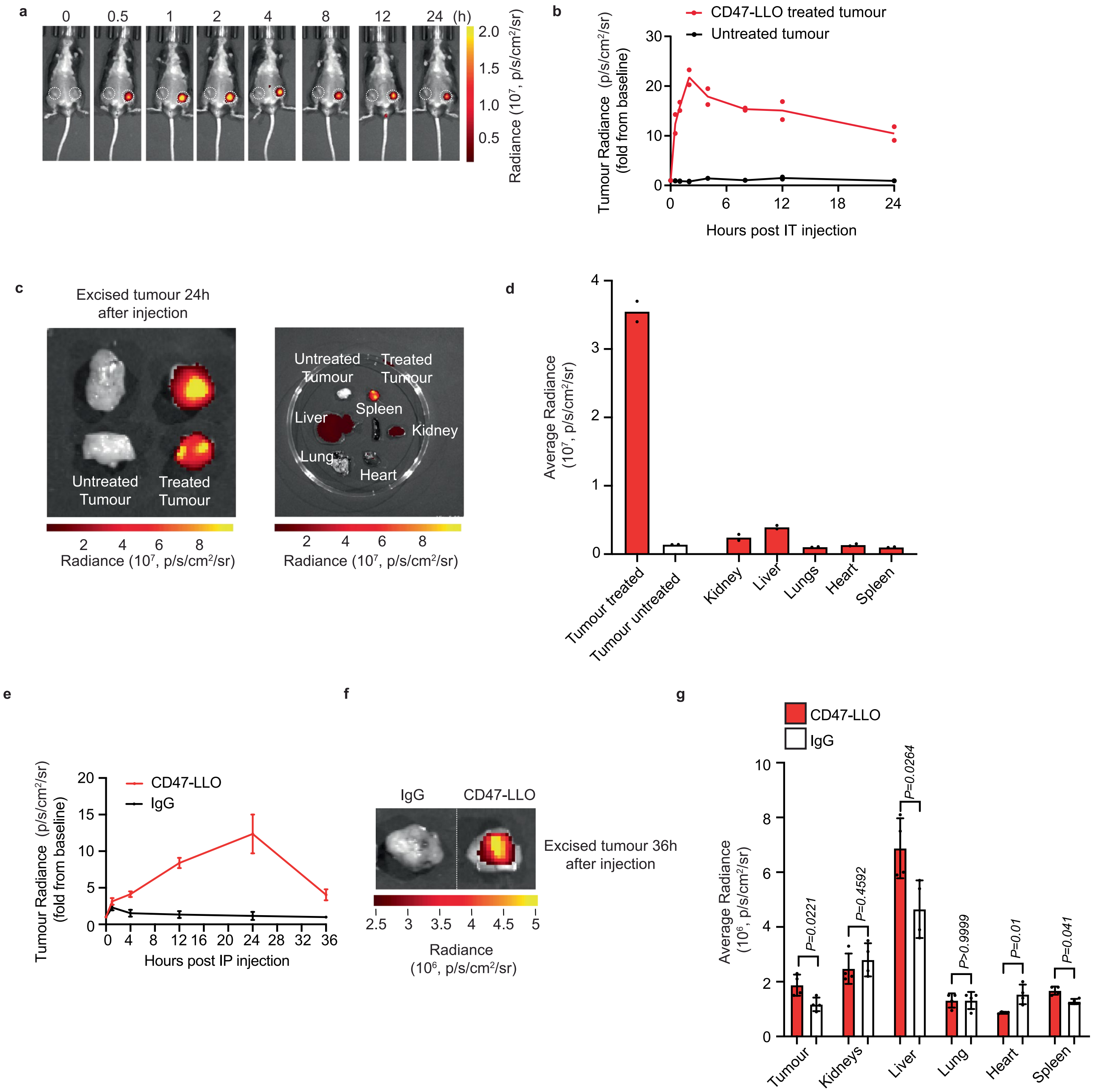

Extended Data Fig. 5 | Biodistribution of CD47-LLO after intratumoural and intraperitoneal administration *in vivo*. **a**, Representative fluorescence images and **b**, quantification of EO771 tumour-bearing mice taken at predetermined times after intratumoural injection of IR800CW-tagged CD47-LLO (25 µg). n = 2 mice. Bilateral tumours enclosed in circles. **c**, *Ex vivo* fluorescence images and **d**, quantification of tumour and major organs collected at 24 h after intratumoural administration. n = 2 mice. **e**, Quantification of EO771 tumours taken at predetermined times after intraperitoneal injection of IR800CW-tagged CD47-LLO (100 µg). n = 4 mice. **f**, *Ex vivo* fluorescence images and **g**, quantification of tumour and major organs collected at 36 h after intraperitoneal administration. n = 4 mice. Data shown represent mean ± s.d. (**b**, **d**, **e**, **g**) analyzed by two-sided unpaired Student's *t* test (**g**).

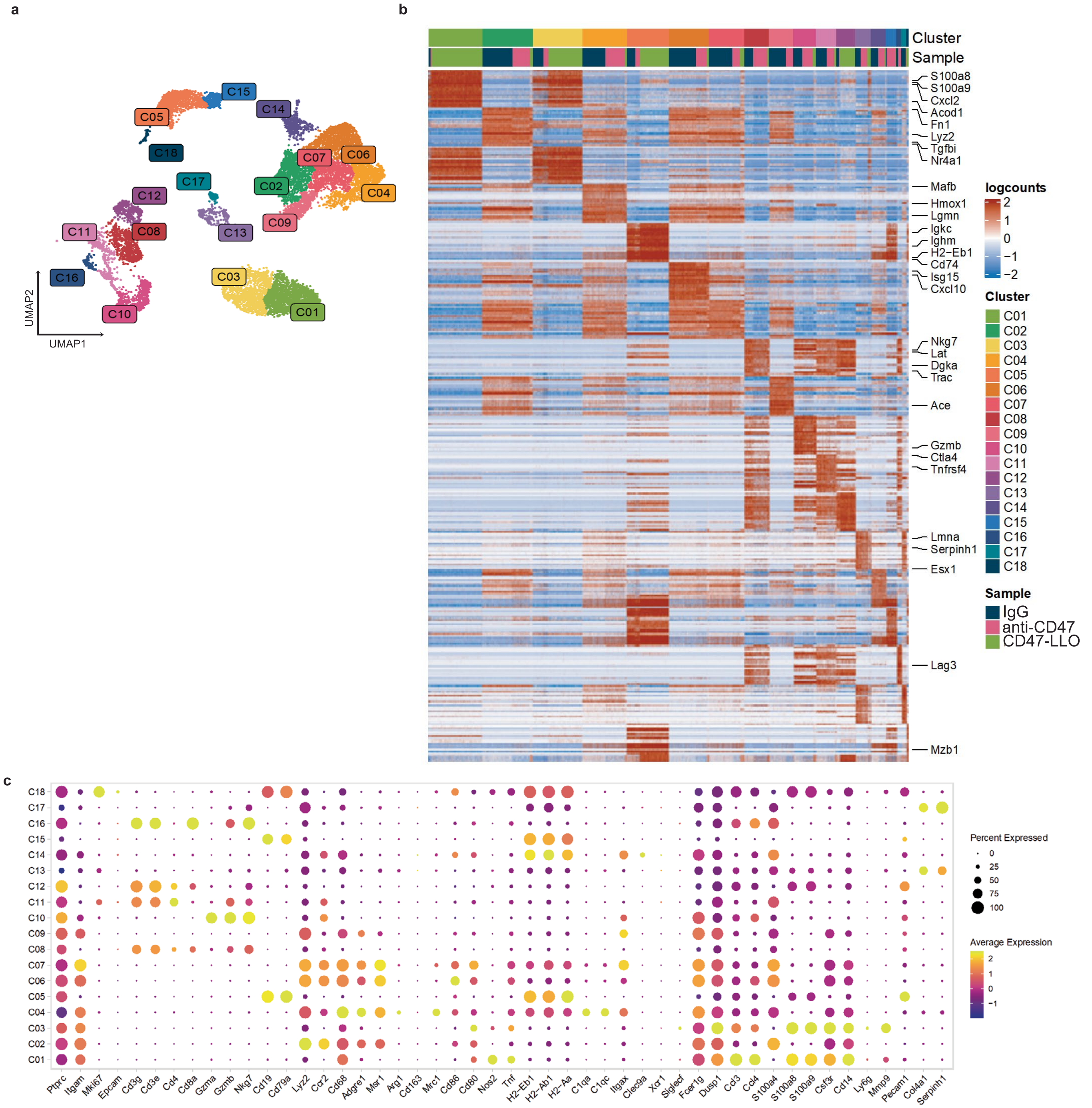

Extended Data Fig. 6 | Tumour-associated CD45+ cells detected by single-cell RNA sequencing. **a**, Uniform manifold approximation and projection (UMAP) of all single cells from 3 treatment groups color-coded by cluster from IgG (n = 3), anti-CD47 (n = 4), or CD47-LLO (n = 4) treated tumours. **b**, Heatmap of 20 differentially expressed genes in clusters, ranked by false discovery rate (FDR) from the 3 treatment groups. **c**, Dot plot showing marker expression for different clusters from the 3 treatment groups. Dot size indicates the percentage of cells in each cluster expressing the gene and colors indicate the average expression levels.

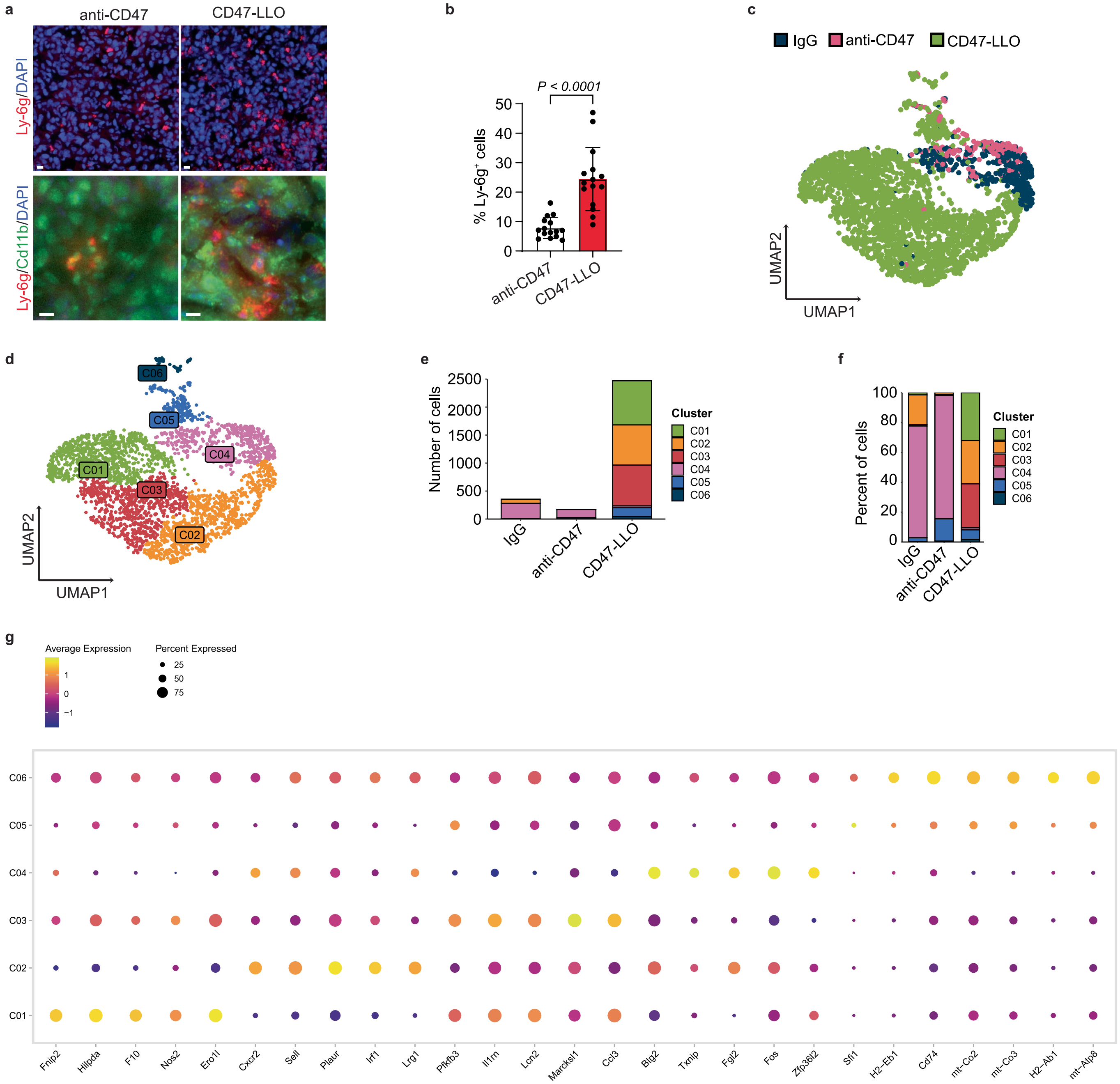

Extended Data Fig. 7 | Tumour-associated neutrophils are enriched in CD47-LLO tumours. a, Representative images show levels of Ly-6g+ (top) and Ly-6g + / Cd11b+ (bottom) cells detected by immunostaining in 4T1Br4 breast tumour frozen tissue sections. Scale bar, 10 µm. **b**, Quantification of Ly-6g$^+$ cells per DAPI$^+$ cells per field of view (*n* = 15 per treatment condition from *n* = 3 biologically independent tumours per condition). **c**, Uniform manifold approximation and projection (UMAP) of only CD45$^+$ granulocytes color-coded by sample from IgG (n = 3), anti-CD47 (n = 4), or CD47-LLO (n = 4) treated tumours. **d**, UMAP projection of only CD45$^+$ granulocytes color-coded by cluster. **e**, Numbers of cells (y-axis) from each cluster (x-axis) color-coded by sample. **f**, Percentage of cells (y-axis) from each cluster (x-axis) color-coded by sample. **g**, Dot plot depicting the top 5 differentially expressed genes per granulocyte cluster. The dot size indicates the percentage of cells in each cluster expressing the gene and colors indicate the average expression levels. Data shown represent mean ± s.d. (**b**) analyzed by two-sided unpaired Student's *t* test.

Extended Data Fig. 8 | See next page for caption.

Extended Data Fig. 8 | Differentially expressed genes define tumour-associated macrophages clusters. a, Dot plot depicting the top 10 differentially expressed genes per macrophage cluster. Dot size indicates the percentage of cells in each cluster expressing the gene and colors indicate the average expression levels from IgG (n = 3), anti-CD47 (n = 4), or CD47-LLO (n = 4) treated tumours. **b**, Dot plot depicting the differential expression of relevant genes for cluster assignments per macrophage cluster from the 3 treatment groups. **c**, Gene set enrichment analysis utilizing the Gene Ontology Biological Process (GOBP) gene set for tumour-associated macrophages with heatmap displaying the ten most upregulated and downregulated pathways in each cluster ranked by their normalized enrichment scores (NES) from the three treatment groups.

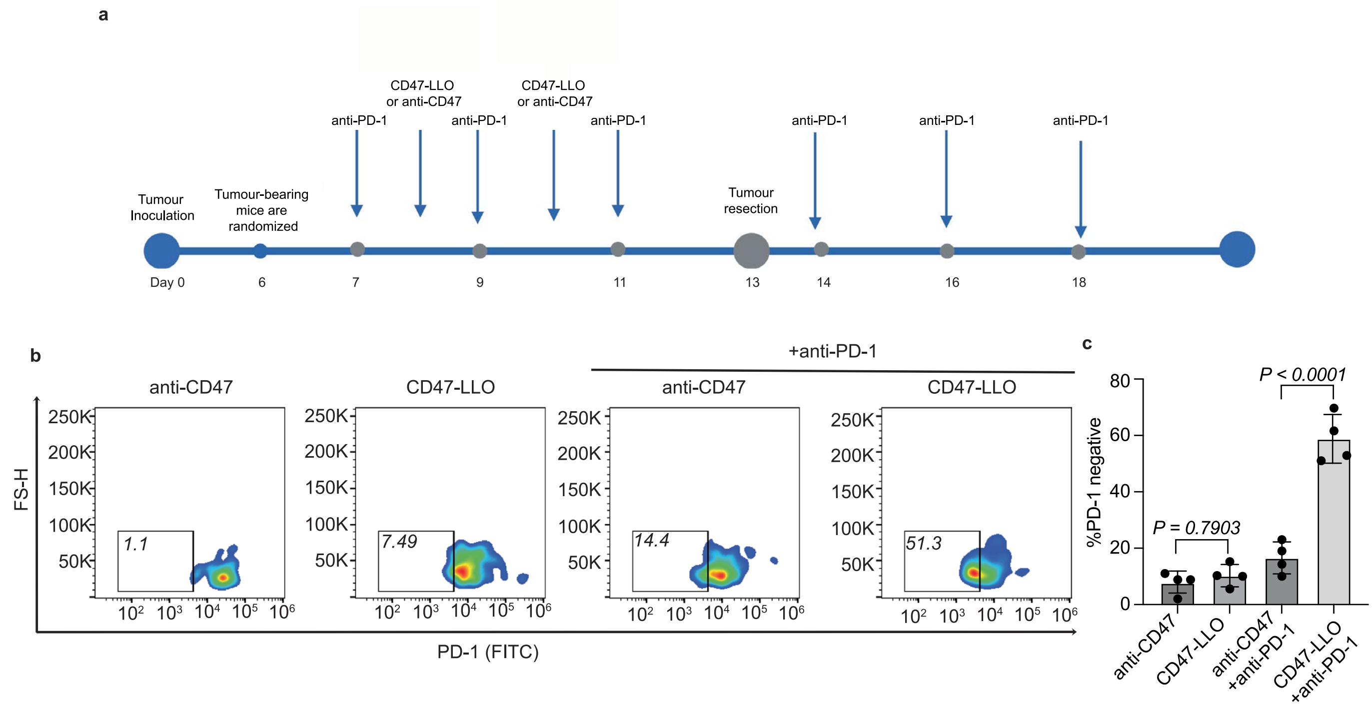

Extended Data Fig. 9 | Tumour-infiltrating CD8 T cells show decreased PD-1 positivity with CD47-LLO and anti-PD-1 treatment. a, Schema for generating *in vivo* syngeneic orthotopic breast cancer models for intraperitoneal injection of CD47-LLO, anti-CD47, and anti-PD1. **b**, Flow cytometry analysis and **c**, quantification of PD-1 negativity in CD8 T cells isolated from 4T1Br4 tumours treated with anti-CD47, CD47-LLO, anti-CD47 + anti-PD-1, or CD47-LLO + anti-PD-1. Data show mean ± s.d. (**c**) analyzed by one-way analysis of variance with Tukey's multiple comparisons test. Data show $n = 4$ mice per treatment group.

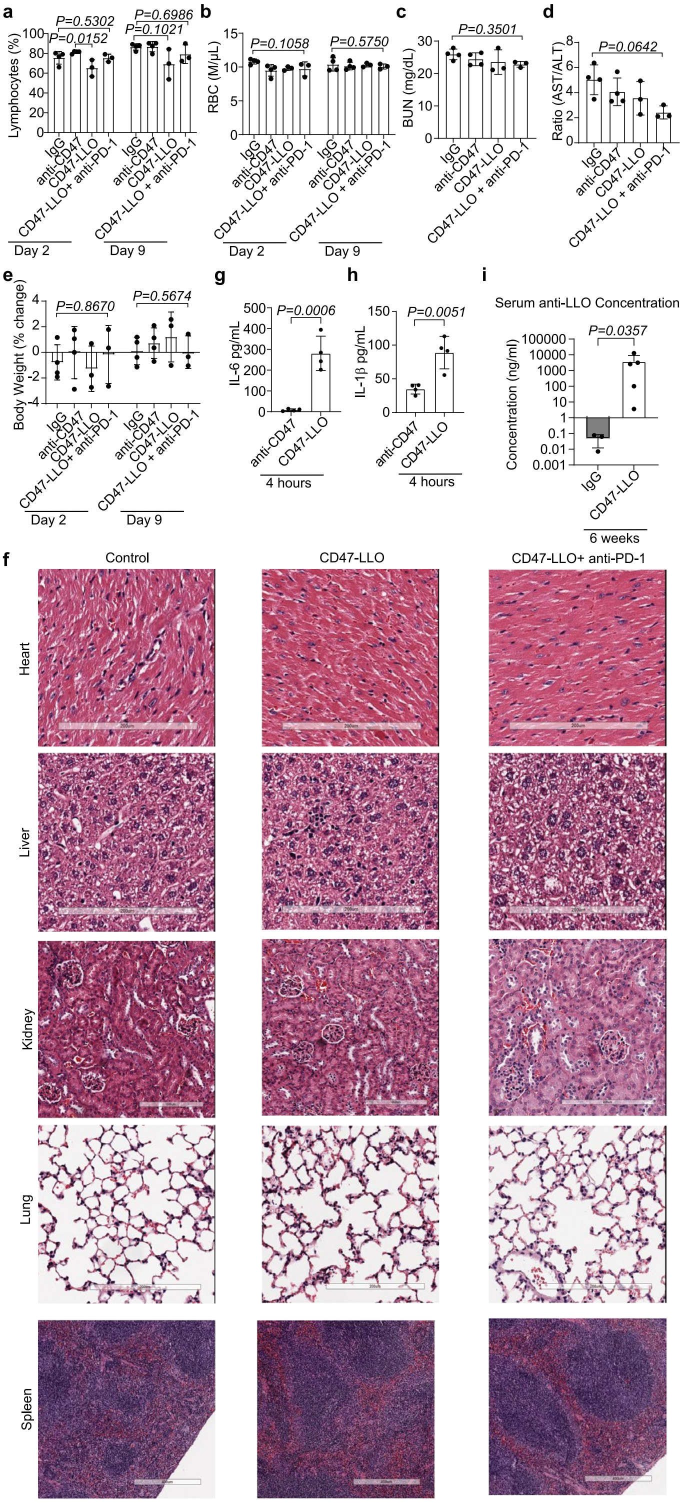

Extended Data Fig. 10 | *In vivo* toxicity of CD47-LLO. a-b, Lymphocyte (**a**) and red blood cell (**b**) counts at day 2 and day 9 after intraperitoneal injection of drug (50 μg IgG, 50 μg anti-CD47, 100 μg CD47-LLO, or 100 μg CD47-LLO + 200 μg anti-PD1). Data show *n* = *4* mice for IgG and anti-CD47 treatment groups and *n* = *3* for other treatment groups. **c**, Serum blood urea nitrogen (BUN) levels and **d**, serum aspartate transaminase / alanine transaminase (AST/ALT) levels at day 9 after drug injection. Data show *n* = *4* mice for IgG and anti-CD47 treatment groups and *n* = *3* for other treatment groups. **e**, Body weight changes in mice at day 2 and day 9 after drug injection. Data show *n* = *4* mice for IgG and anti-CD47 treatment groups and *n* = *3* for other treatment groups. **f**, Hematoxylin and eosin staining of paraffin sections of major organs two days after intraperitoneal injection of CD47-LLO or CD47-LLO and anti-PD-1. Experiment was repeated independently n = 3 times with similar results; a representative result is shown. Scale bar, 200 mm. **g**, Serum IL-6 levels at 4 hours after drug injection measured by enzyme-linked immunosorbent assay (ELISA). Data show *n* = *4* C57BL6 mice per treatment group. **h**, Serum IL-1β levels at 4 hours after drug injection measured by ELISA. Data show *n* = *4* C57BL6 mice per treatment group. **i**, Serum concentrations of anti-LLO antibody at 6 weeks after drug injection by sandwich immunogenicity assay. Data show *n* = *3* mice per IgG treatment group and *n* = *5* mice per CD47-LLO treatment group. Data shown represent mean ± s.d. (**a, b, c, d, e, g, h, i**) analyzed by one-way analysis of variance with Tukey's multiple comparisons test (**a, b, c, d, e**) or two-sided unpaired Student's *t* test (**g, h, i**).

nature portfolio

Corresponding author(s): Wen Jiang, Betty Kim

Last updated by author(s): Jan 15, 2025

Reporting Summary

Nature Portfolio wishes to improve the reproducibility of the work that we publish. This form provides structure for consistency and transparency in reporting. For further information on Nature Portfolio policies, see our Editorial Policies and the Editorial Policy Checklist.

Statistics

For all statistical analyses, confirm that the following items are present in the figure legend, table legend, main text, or Methods section.

n/a	Confirmed	
☐	☒	The exact sample size (*n*) for each experimental group/condition, given as a discrete number and unit of measurement
☐	☒	A statement on whether measurements were taken from distinct samples or whether the same sample was measured repeatedly
☐	☒	The statistical test(s) used AND whether they are one- or two-sided *Only common tests should be described solely by name; describe more complex techniques in the Methods section.*
☐	☒	A description of all covariates tested
☐	☒	A description of any assumptions or corrections, such as tests of normality and adjustment for multiple comparisons
☐	☒	A full description of the statistical parameters including central tendency (e.g. means) or other basic estimates (e.g. regression coefficient) AND variation (e.g. standard deviation) or associated estimates of uncertainty (e.g. confidence intervals)
☐	☒	For null hypothesis testing, the test statistic (e.g. *F*, *t*, *r*) with confidence intervals, effect sizes, degrees of freedom and *P* value noted *Give P values as exact values whenever suitable.*
☒	☐	For Bayesian analysis, information on the choice of priors and Markov chain Monte Carlo settings
☒	☐	For hierarchical and complex designs, identification of the appropriate level for tests and full reporting of outcomes
☒	☐	Estimates of effect sizes (e.g. Cohen's *d*, Pearson's *r*), indicating how they were calculated

Our web collection on statistics for biologists contains articles on many of the points above.

Software and code

Policy information about availability of computer code

Data collection	Living Image Software 4.7, BD Accuri C6 software v227
Data analysis	FlowJo 10.7.2, GraphPad Prism 10.0.3, Microsoft Excel 365, BD Accuri C6 software v227, ImageJ 1.51, Cell Ranger v.7.1.0, R v.4.1.2, Seurat v.4.3.0.1, DESeq2 vl.40.2, Living Image Software 4.7, Aura 4.0, Icy Software v3.0, CellChat v1.6.1

For manuscripts utilizing custom algorithms or software that are central to the research but not yet described in published literature, software must be made available to editors and reviewers. We strongly encourage code deposition in a community repository (e.g. GitHub). See the Nature Portfolio guidelines for submitting code & software for further information.

Data

Policy information about availability of data

All manuscripts must include a data availability statement. This statement should provide the following information, where applicable:

- Accession codes, unique identifiers, or web links for publicly available datasets
- A description of any restrictions on data availability
- For clinical datasets or third party data, please ensure that the statement adheres to our policy

The authors declare that data supporting the findings of this study are available within the article and its supplementary information. The sequencing data has been deposited in the National Center for Biotechnology Information Gene Expression Omnibus database under a publicly available accession number GSE255937. The

GRCm39-based mouse reference genome is available from the UCSC Genome Browser. Source data for Fig 1, 2, 3, 4, 5, 6, 7, 8 and Extended Data Data Fig 1, 2, 3, 4, 5, 7, 9, 10 have been provided as Source Data files. All equipment and reagents are commercially available and are described in the Methods section.

Research involving human participants, their data, or biological material

Policy information about studies with human participants or human data. See also policy information about sex, gender (identity/presentation), and sexual orientation and race, ethnicity and racism.

Reporting on sex and gender	N/A
Reporting on race, ethnicity, or other socially relevant groupings	N/A
Population characteristics	N/A
Recruitment	N/A
Ethics oversight	N/A

Note that full information on the approval of the study protocol must also be provided in the manuscript.

Field-specific reporting

Please select the one below that is the best fit for your research. If you are not sure, read the appropriate sections before making your selection.

☒ Life sciences ☐ Behavioural & social sciences ☐ Ecological, evolutionary & environmental sciences

For a reference copy of the document with all sections, see nature.com/documents/nr-reporting-summary-flat.pdf

Life sciences study design

All studies must disclose on these points even when the disclosure is negative.

Sample size	Group sizes for in vivo experiments were selected empirically based on previous results of the intra-group variability in tumor growth upon similar treatments. For in vitro experiments, group sizes were selected on the basis of previous publication and prior knowledge of variation and were replicated at least 3 independent experiments (Ref:, Nature Nanotechnology volume 17, pages1332–1341 (2022); Nature Nanotechnology volume 17, pages891–899 (2022)).
Data exclusions	For mouse tumor treatment experiments, mice that spontaneously rejected tumors were excluded from randomization and treatment. No other data were excluded.
Replication	All experiments were repeated biologically, and all results were reproducible. Replicates were used in all experiments as noted in the figure legend or methods and were performed over a few weeks or months.
Randomization	Age and sex-matched animals were used for individual experiments. Mice were randomized prior to treatment when the tumor reached a certain size (as described in the Methods section). For experiments without animals, there was no randomization employed as these in vitro experiments are observational.
Blinding	In vivo tumor engraftment and grouping were conducted randomly before treatment. Fully blinded experiments were not performed due to insufficient personnel availability to accommodate requirements for cage labeling and staffing needs.

Reporting for specific materials, systems and methods

We require information from authors about some types of materials, experimental systems and methods used in many studies. Here, indicate whether each material, system or method listed is relevant to your study. If you are not sure if a list item applies to your research, read the appropriate section before selecting a response.

Materials & experimental systems

n/a	Involved in the study
☐	☒ Antibodies
☐	☒ Eukaryotic cell lines
☒	☐ Palaeontology and archaeology
☐	☒ Animals and other organisms
☒	☐ Clinical data
☒	☐ Dual use research of concern
☐	☐ Plants

Methods

n/a	Involved in the study
☒	☐ ChIP-seq
☐	☒ Flow cytometry
☒	☐ MRI-based neuroimaging

Antibodies

Antibodies used

Antibodies or tetramer used for flow cytometry

anti-CD16/CD32 antibody (Clone: 2.4G2, Catalog #: BE0307, Bio X Cell, USA. Manufacturer verified application is in vitro Fc receptor blocking.
anti-mouse phospho-STING (Ser365) (Clone: D8F4W, Catalog #: 72971, Cell Signaling Technology, USA)
FITC anti-mouse CD279 (PD-1) (Clone: 29F.1A12, Catalog #: 135213, Biolegend, USA)
PE/Cyanine7 anti-mouse CD45 (Clone: 30-F11, Catalog #: 10311325, Biolegend, USA)
APC anti-mouse CD90.2 (Thy1.2) (Clone: 30-H12, Catalog #: 105312, Biolegend, USA)
Alexa Fluor® 700 anti-mouse CD4 (Clone: GK1.5 , Catalog #: 100430, BioLegend, USA)
PE anti-mouse CD8a (Clone: 53-6.7, Catalog #: 100708, BioLegend, USA)
FITC anti-mouse/human CD11b (Clone: M1/70, Catalog #: 101205, Biolegend, USA)
BV650™ anti-mouse CD86 (Clone: GL-1, Catalog #: 105035, Biolegend USA)
APC anti-mouse CD206 antibody (Clone: C068C2, Catalog #: 141707, Biolegend, USA)
Tetramer/BV421-H2Kb OVA (SIINFEKL) (Catalog #: TB-5001-4, MBL International Corporation, USA)
PE anti-mouse CD45 (Clone: 30-F11, Catalog #: 103105, Biolegend, USA)
PE anti-mouse H-2Kd/H-2Dd Antibody (Clone: 34-1-2S, Catalog #: 114708200, Biolegend, USA)
PE/Cyanine7 anti-mouse CD11c (Clone: N418 Catalog #: 117317, Biolegend, USA)
BV421 anti-mouse CD11b antibody (Clone: BM8, Catalog #: 123132, Biolegend, USA)
PE anti-mouse CD11b antibody (Clone: M1/70, Catalog #: 101207, Biolegend, USA)
APC anti-mouse H-2Kd/H-2Dd-APC (Clone: 34-1-2S, Catalog #: 114714, Biolegend, USA)
APC/Fire 750 anti-mouse CD3 (Clone: 17A2, Catalog #: 100248, BioLegend, USA)
PE anti-mouse CD86 antibody (Clone: GL-1, Catalog #: 105008, Biolegend, USA)
APC anti-mouse SIINFEKL/H-2Kb antibody (Clone: 25-D1.16, Catalog #: 41606, Biolegend, USA)

Antibodies for surface staining were used at a 1:100 dilution, for intracellular staining at a 1:50 dilution.

Antibodies used for western blotting and immunofluorescence staining
β-actin Rabbit pAb (Catalog #4967, Cell Signaling Technology, USA), Dilution: 1:500;
p-STING (Ser366) pAb (Catalog # PA5-105674, ThermoFisher Scientific, USA), Dilution: 1:200;
STING (D2P2F) Rabbit mAb (Catalog #: 13647, Cell Signaling Technology, USA), Dilution: 1:200;
anti-mouse CD8 (Clone: EPR22331-54, Catalog #: ab228965, Abcam, UK), Dilution: 1:200;
anti-F4/80 antibody [CI:A3-1] - Macrophage Marker (Clone: CI:A3-1, Catalog #: ab6640, Abcam, UK), Dilution: 1:100;
FITC-tagged Goat anti-rabbit secondary Ab (Catalog #: 31573, ThermoFisher Scientific, USA), Dilution: 1:1000;
FITC-tagged Donkey anti-mouse secondary Ab (Catalog #: A16012, ThermoFisher Scientific, USA), Dilution: 1:1000;
Alexa Fluor 647-tagged Goat anti-rabbit secondary Ab (Catalog # A-21245, ThermoFisher Scientific, USA), Dilution: 1:1000;
Alexa Fluor 546-tagged Goat anti-rat secondary Ab (Biolegend, USA), Dilution: 1:1000;
anti-mouse CD4 (RM4-5) FITC Conjugate (Catalog #: 96127S, Cell Signaling Technology, USA), Dilution: 1:100;
CD11c Monoclonal Antibody (N418), eBioscience™ (Catalog #: 14-0114-82, ThermoFisher Scientific, USA), Dilution: 1:100
Anti-Ly6g + Ly6c antibody (Clone: B6-8C5, Catalog #: ab25377, Abcam, UK), Dilution 1:200.
cGAS (D3O8O) Rabbit mAb (Catalog #: 31659, Cell Signaling Technology, USA), Dilution: 1:200;

Antibody for in vivo study
InVivoMAb anti-mouse PD1 (CD279) (Clone: RMP1-14, Catalog #: BE0146, BioXcell, USA)
InVivoMAb anti-mouse CD8α (Clone: YTS 169.4, Catalog #: BE0117, BioXcell, USA)
InVivoMAb anti-mouse CSF1R (Clone: AFS98 Catalog #: BE0213, BioXcell, USA)
InVivoMAb anti-mouse CD47 (Clone: MIAP410, Catalog #: BE0283, BioXcell, USA)
InVivoMAb anti-mouse IgG1 (Clone: MOPC-21, Catalog #: BE0083, BioXcell, USA)

Validation

For antibodies used in flow cytometry, each antibody has been validated by the manufacturer for use to detect mouse species targets. These antibodies are additionally validated and routinely used in our laboratory with good reproducibility. Detailed validation information for each antibody is available at the following websites:

1. anti-CD16/CD32 antibody (Clone: 2.4G2, Catalog #: BE0307): https://bioxcell.com/invivomab-anti-mouse-cd16-cd32-be0307
2. anti-mouse phospho-STING (Ser365) (Clone: D8F4W, Catalog #: 72971) https://www.cellsignal.com/products/primary-antibodies/phospho-sting-ser365-d8f4w-rabbit-mab/72971?srsltid=AfmBOooTf6IW4MAKftcjuD1MLBle32eJyEKCuhbUbk-8sgI_zZ8DjVKN
3. FITC anti-mouse CD279 (PD-1) (Clone: 29F.1A12, Catalog #: 135213) https://www.biolegend.com/fr-ch/products/fitc-anti-mouse-cd279-pd-1-antibody-7004
4. PE/Cyanine7 anti-mouse CD45 (Clone: 30-F11, Catalog #: 10311325, Biolegend, USA) https://www.biolegend.com/en-ie/products/

pe-cyanine7-anti-mouse-cd45-antibody-1903?GroupID=BLG1932

5. APC anti-mouse CD90.2 (Thy1.2) (Clone: 30-H12, Catalog #: 105312, Biolegend, USA) https://www.biolegend.com/en-us/products/purified-anti-mouse-cd90-2-thy1-2-antibody-107
6. Alexa Fluor® 700 anti-mouse CD4 (Clone: GK1.5 , Catalog #: 100430, BioLegend, USA) https://www.biolegend.com/nl-be/products/alexa-fluor-700-anti-mouse-cd4-antibody-3385
7. PE anti-mouse CD8a (Clone: 53-6.7, Catalog #: 100708, BioLegend, USA) https://www.biolegend.com/fr-ch/products/pe-anti-mouse-cd8a-antibody-155?GroupID=BLG2559
8. FITC anti-mouse/human CD11b (Clone: M1/70, Catalog #: 101205, Biolegend, USA) https://www.biolegend.com/en-ie/products/fitc-anti-mouse-human-cd11b-antibody-347?GroupID=BLG10660
9. BV650™ anti-mouse CD86 (Clone: GL-1, Catalog #: 105035, Biolegend USA) https://www.biolegend.com/de-de/products/brilliant-violet-650-anti-mouse-cd86-antibody-7643
10. APC anti-mouse CD206 antibody (Clone: C068C2, Catalog #: 141707, Biolegend, USA) https://www.biolegend.com/en-ie/products/apc-anti-mouse-cd206-mmr-antibody-7425?GroupID=BLG9506
11. Tetramer/BV421-H2Kb OVA (SIINFEKL) (Catalog #: TB-5001-4, MBL International Corporation, USA) https://products.mblintl.com/products/tb-5001-4/
12. PE anti-mouse CD45 (Clone: 30-F11, Catalog #: 103105, Biolegend, USA) https://www.biolegend.com/nl-nl/products/pe-anti-mouse-cd45-antibody-100
13. PE anti-mouse H-2Kd/H-2Dd Antibody (Clone: 34-1-2S, Catalog #: 114708200, Biolegend, USA) https://www.biolegend.com/ja-jp/products/pe-anti-mouse-h-2kd-h-2dd-antibody-1887
14. PE/Cyanine7 anti-mouse CD11c (Clone: N418 Catalog #: 117317, Biolegend, USA) https://www.biolegend.com/fr-ch/products/pe-cyanine7-anti-mouse-cd11c-antibody-3086?GroupID=BLG11937
15. BV421 anti-mouse CD11b antibody (Clone: BM8, Catalog #: 123132, Biolegend, USA) https://www.biolegend.com/fr-ch/products/brilliant-violet-421-anti-mouse-f4-80-antibody-7199
16. PE anti-mouse CD11b antibody (Clone: M1/70, Catalog #: 101207, Biolegend, USA) https://www.biolegend.com/fr-ch/products/pe-anti-mouse-human-cd11b-antibody-349
17. APC anti-mouse H-2Kd/H-2Dd-APC (Clone: 34-1-2S, Catalog #: 114714, Biolegend, USA) https://www.biolegend.com/en-ie/products/apc-anti-mouse-h-2kd-h-2dd-antibody-15819
18. APC/Fire 750 anti-mouse CD3 (Clone: 17A2, Catalog #: 100248, BioLegend, USA) https://www.biolegend.com/fr-lu/products/apc-fire-750-anti-mouse-cd3-antibody-13052
19. PE anti-mouse CD86 antibody (Clone: GL-1, Catalog #: 105008, Biolegend, USA) https://www.biolegend.com/ja-jp/products/pe-anti-mouse-cd86-antibody-256
20. APC anti-mouse SIINFEKL/H-2Kb antibody (Clone: 25-D1.16, Catalog #: 41606, Biolegend, USA) https://www.biolegend.com/en-gb/clone-search/apc-anti-mouse-h-2kb-bound-to-siinfekl-antibody-7882?GroupID=BLG9387

For antibodies used for western blotting and immunofluorescence staining, each antibody has been validated by the manufacturer for use to detect mouse species targets. Detailed validation information for each antibody is included at the following websites:

1. β-actin Rabbit pAb (Catalog #4967, Cell Signaling Technology, USA) https://www.cellsignal.com/products/primary-antibodies/b-actin-antibody/4967?srsltid=AfmBOoqM_Tf03gDMf_7bbT2G2CArjibqj4YnuJs4wOrOtTirP7Vix1vu
2. p-STING (Ser366) pAb (Catalog # PA5-105674, ThermoFisher Scientific, USA) https://www.thermofisher.com/antibody/product/Phospho-STING-Ser366-Antibody-Polyclonal/PA5-105674
3. STING (D2P2F) Rabbit mAb (Catalog #: 13647, Cell Signaling Technology, USA) https://www.cellsignal.com/products/primary-antibodies/sting-d2p2f-rabbit-mab/13647?srsltid=AfmBOooH5CiAq0WMe_uvBoCA8rvTAcrJ1jwqkTHalGBOs72at-zHnPx9
4. anti-mouse CD8 (Clone: EPR22331-54, Catalog #: ab228965, Abcam, UK) https://www.abcam.com/en-us/products/primary-antibodies/cd8-beta-antibody-epr22331-54-ab228965?srsltid=AfmBOoo2w6xg-6TbvcW3C5qWTegOG4IsslTrlVEf89z13vfnR5VCfL9r#tab=datasheet
5. anti-F4/80 antibody [CI:A3-1] - Macrophage Marker (Clone: CI:A3-1, Catalog #: ab6640, Abcam, UK) https://www.abcam.com/en-us/products/primary-antibodies/f4-80-antibody-cia3-1-macrophage-marker-ab6640?srsltid=AfmBOooFMh7we5GLqR7UTzcxaKRbWd2xjwwdmJIpboe9Cmk_osEsiG-B
6. FITC-tagged Goat anti-rabbit secondary Ab (Catalog #: 31573, ThermoFisher Scientific, USA) https://www.thermofisher.com/antibody/product/Goat-anti-Rabbit-IgG-F-ab-2-Secondary-Antibody-Polyclonal/31573
7. FITC-tagged Donkey anti-mouse secondary Ab (Catalog #: A16012, ThermoFisher Scientific, USA) https://www.thermofisher.com/antibody/product/Donkey-anti-Mouse-IgG-H-L-Secondary-Antibody-Polyclonal/A16012
8. Alexa Fluor 647-tagged Goat anti-rabbit secondary Ab (Catalog # A-21245, ThermoFisher Scientific, USA) https://www.thermofisher.com/antibody/product/Goat-anti-Rabbit-IgG-H-L-Highly-Cross-Adsorbed-Secondary-Antibody-Polyclonal/A-21245
9. Alexa Fluor 546-tagged Goat anti-rat secondary Ab (Biolegend, USA) https://www.biolegend.com/fr-ch/products/alexa-fluor-594-goat-anti-rat-igg-minimal-x-reactivity-9455
10. anti-mouse CD4 (RM4-5) FITC Conjugate (Catalog #: 96127S, Cell Signaling Technology, USA) https://www.cellsignal.com/products/antibody-conjugates/cd4-rm4-5-rat-mab-fitc-conjugate/96127?srsltid=AfmBOopHjuID7cR0a-W9NdKAoinQC2RFLHuDMOEN-a9qPfd5s5QHzLpj
11. CD11c Monoclonal Antibody (N418), eBioscience™ (Catalog # 14-0114-82, ThermoFisher Scientific, USA) https://www.thermofisher.com/antibody/product/CD11c-Antibody-clone-N418-Monoclonal/14-0114-82
12. Anti-Ly6g + Ly6c antibody (Clone: B6-8C5, Catalog #: ab25377, Abcam, UK) https://www.abcam.com/en-us/products/primary-antibodies/ly6g-ly6c-antibody-rb6-8c5-ab25377?productwalltab=abreviews
13. cGAS (D3O8O) Rabbit mAb (Catalog #: 31659, Cell Signaling Technology, USA) https://www.cellsignal.com/products/primary-antibodies/cgas-d3o8o-rabbit-mab/31659?srsltid=AfmBOopWOPJX8Yjsu0FXYVWFnTIdf6DzqpZqqjj7YaBtt3QTHWYLFwiY

For antibodies used to deplete cells or blockade signals in vivo, detailed validation information for each antibody is available at the following sites:
1. InVivoMAb anti-mouse PD1 (CD279) (Clone: RMP1-14, Catalog #: BE0146, BioXcell, USA) https://bioxcell.com/invivomab-anti-mouse-pd-1-cd279-be0146
2. InVivoMAb anti-mouse CD8α (Clone: YTS 169.4, Catalog #: BE0117, BioXcell, USA), https://bioxcell.com/invivomab-anti-mouse-cd8-alpha-be0117
3. InVivoMAb anti-mouse CSF1R (Clone: AFS98 Catalog #: BE0213, BioXcell, USA), https://bioxcell.com/invivomab-anti-mouse-csf1r-cd115-be0213
4. InVivoMAb anti-mouse CD47 (Clone: MIAP410, Catalog #: BE0283, BioXcell, USA) https://bioxcell.com/invivomab-anti-mouse-

human-rat-cd47-iap-be0283
5. InVivoMAb anti-mouse IgG1 (Clone: MOPC-21, Catalog #: BE0083, BioXcell, USA) https://bioxcell.com/invivomab-mouse-igg1-isotype-control-unknown-specificity-be0083

Eukaryotic cell lines

Policy information about cell lines and Sex and Gender in Research

Cell line source(s)	The mouse mammary breast carcinoma 4T1Br4 cell line was obtained from the American Type Culture Collection (ATCC). The mouse melanoma D4M3A cell line was a gift from D. Fisher (Massachusetts General Hospital) and is commercially available from Sigma-Aldrich (Catalog #: SCC428). The mouse mammary carcinoma cell line EO771 was obtained from CH3 Biosystems. The mouse KPC cell line was a gift from D. Jiang (MD Anderson Cancer Center) and is commercially available through CancerTools.org (Catalog #: 153474).
Authentication	The EO771, KPC, and 4T1 cell lines were authenticated by short tandem repeat (STR) profiling. D4M.3A cells have been validated through whole exome sequencing.
Mycoplasma contamination	All cell lines were tested negative for mycoplasma contamination.
Commonly misidentified lines (See ICLAC register)	No misidentified cell lines were used in this study.

Animals and other research organisms

Policy information about studies involving animals; ARRIVE guidelines recommended for reporting animal research, and Sex and Gender in Research

Laboratory animals	C57BL/6J, C57BL/6J-Stinglgt/J, BALB/cJ, OT-I (C57BL/6-Tg(TcraTcrb)1100Mjb/J) mice were purchased from The Jackson Laboratory. All mice for orthotopic breast tumor models were female and aged 6-8 weeks (n=197). All mice for orthotopic melanoma tumor models were male and aged 6-8 weeks (n=13).
Wild animals	No wild animals were used for this study.
Reporting on sex	Sex was reported in the methods and/or figure legends.
Field-collected samples	Study did not involve field-collected samples.
Ethics oversight	All mouse experiment protocols were reviewed and approved by the Institutional Animal Care and Use Committee of The University of Texas MD Anderson Cancer Center (#00002163), The University of Texas Southwestern Medical Center (#2018-102602). In line with to animal ethics guidelines, the mice were humanely euthanized when the tumour diameter reached 20mm or when the animals displayed indicators of distress that aligned with the established institutional standards for initiating early euthanasia in all experiments of tumour inhibition. Signs for euthanasia include laboured breathing, abnormal movement, hypothermia, hunched posture, and more than 20% of body weight loss compared with baseline. Maximal tumour diameter was not exceeded in this study.

Note that full information on the approval of the study protocol must also be provided in the manuscript.

Plants

Seed stocks	*Report on the source of all seed stocks or other plant material used. If applicable, state the seed stock centre and catalogue number. If plant specimens were collected from the field, describe the collection location, date and sampling procedures.*
Novel plant genotypes	*Describe the methods by which all novel plant genotypes were produced. This includes those generated by transgenic approaches, gene editing, chemical/radiation-based mutagenesis and hybridization. For transgenic lines, describe the transformation method, the number of independent lines analyzed and the generation upon which experiments were performed. For gene-edited lines, describe the editor used, the endogenous sequence targeted for editing, the targeting guide RNA sequence (if applicable) and how the editor was applied.*
Authentication	*Describe any authentication procedures for each seed stock used or novel genotype generated. Describe any experiments used to assess the effect of a mutation and, where applicable, how potential secondary effects (e.g. second site T-DNA insertions, mosiacism, off-target gene editing) were examined.*

Flow Cytometry

Plots

Confirm that:

☒ The axis labels state the marker and fluorochrome used (e.g. CD4-FITC).

☒ The axis scales are clearly visible. Include numbers along axes only for bottom left plot of group (a 'group' is an analysis of identical markers).

☒ All plots are contour plots with outliers or pseudocolor plots.

☒ A numerical value for number of cells or percentage (with statistics) is provided.

Methodology

Sample preparation	Flow cytometry. The treated mice from each group were euthanized on the indicated days post tumour inoculation, and the perfused tumour or spleen tissues were collected and digested in 200 U ml-1 collagenase D, 1.6 U ml-1 dispase and 15 U ml-1 DNase I in 10 mmol l-1 HEPES buffer at 37 °C for 30 min to obtain the cell suspensions. The dissociated cells were then filtered through a 70-µm nylon cell strainer and collected for the following analyses. CD45+ cells were isolated EasySep™ Mouse TIL (CD45) Positive Selection Kit (Catalog # 100-0350). Tumour-associated macrophages (TAMs), CD8+ T cells, and CD4 + T cells were isolated for flow cytometry analysis as follows. Cells were dissociated and first blocked with anti-CD16/CD32 (Bio X Cell, Cat # BE0307, dilution of 1:200) for 15 min to avoid nonspecific binding to the Fc receptor. The cells were stained by the antibodies indicated above for 1h at 4 degree or 20 min at room temperature. For other analyses, cells were stained separately with different antibodies (anti-CD8a-PE, dilution of 1:200; Thy1.2-APC, dilution of 1:200; anti-CD4-AF700, dilution of 1:200; anti-CD11b-PE, dilution 1:200; anti-CD11b-BV421, dilution 1:200; phospho-STING, dilution 1:50; CD206-APC, dilution 1:200; CD86-PE, dilution 1:200; ova-tetramer-BV421, dilution 1:200 according to the manufacturer's instructions. Both CD8+ T and CD4+ T cells are also gated as CD3/Thy1.2 positive.
Instrument	The cells were processed on a BD Accuri C6, BD FACS Calibur, Beckman Coulter Gallios flow cytometer, or Invitrogen Attune flow cytometer.
Software	Results were analyzed by FlowJo 10.7.2 or BD Accuri C6 software v227.
Cell population abundance	The mouse tumor cells were sorted by FACS to isolate the CD45+ populations. The sorted population abundance was between 1-30% of the total cells. Post-sort fraction was analyzed by single cell RNA-sequencing. The cell populations included in the final analysis all had CD45 expression.
Gating strategy	Gating strategies are provided in the supplementary figures. FSC/SSC gating was used to exclude dead cells and debris. The positive or negative populations were determined by comparing the stained sample with unstained control. The population with fluorescence intensity higher than that of the unstained control is considered positive and the other population is considered negative.

☒ Tick this box to confirm that a figure exemplifying the gating strategy is provided in the Supplementary Information.